BULLETIN OF MATERIALS SCIENCE AND METALLURGY

Volume 1 I Issue 2 I Pages 1-25 I JUN 2024

ONLINE ISSN:3023-6509

bulletinofmsm.org/

BULLETIN OF MATERIALS SCIENCE AND METALLURGY

BULLETIN OF MATERIALS SCIENCE AND METALLURGY

BULLETIN OF MATERIALS SCIENCE AND METALLURGY

BULLETIN OF
MATERIALS SCIENCE AND METALLURGY

CONTENTS

BMSM

Bulletin of Materials Science & Metallurgy

Periodical Scientific Journal of UCTEA Chamber of Metallurgical and Materials Engineers

Volume 1, Issue 2, 2024, Pages 1-10 Received: 21 March 2024 Accepted: 29 May 2024

Research Article

Effect Of Heat Input On Microstructure And Mechanical Properties Of Tig Welded Aisi 318ln Stainless Steel Plates

Muhammed M. Arslan[a,*], Gürel Çam[b,*]

[a]Iskenderun Technical University, Institute of Engineering and Sciences, Iskenderun-Hatay, Türkiye

[b]Iskenderun Technical University, Faculty of Engineering and natural Sciences, Department of Mechanical Engineering, Iskenderun-Hatay, Türkiye

*Corresponding author's email: gurel.cam@iste.edu.tr

Abstract

Duplex stainless steel is the type with the best corrosion resistance among all types of stainless steel. However, their cost is higher than other stainless steels. Therefore, it is more widely used in areas where the risk of corrosion is high. Therefore, the most common use of duplex stainless steel is in the petrochemical industry. In this sector, where chemicals with high abrasive power are used, duplex stainless steel is used for both the transport and storage of chemicals. Welding is an indispensable fabrication method in these applications. Therefore, there is a need for reliable welding procedures that will not adversely affect the mechanical properties and corrosion behavior of these steels in the weld zone.

In this study, the microstructural evolution and mechanical properties of the 3 mm thick SAF 2205 (AISI 318LN) duplex stainless steel welded joints fabricated by the gas tungsten arc welding method using an ER2209 filler wire were investigated. The microstructures formed in the weld area were examined in detail with an optical microscope. The mechanical properties and welding performance values of the joints obtained were determined by tensile test and microhardness measurements. In addition, the effect of heat input on the microstructure and mechanical properties of welded joints was also investigated.

Keywords

SAF 2205, AISI 318N, TIG, Duplex Stainless Steel, Microstructural Evolution, Weld Performance

1. Introduction

Duplex stainless-steel plates are generally produced by cold rolling in the final stage. Thanks to the ferrite/austenite balance in the microstructure of duplex stainless steels, these materials show high mechanical properties [1-4]. The most important advantage of these steels compared to austenitic stainless steels is that their yield strength is twice as high. In addition, these steels have superior corrosion resistance (high resistance to stress corrosion cracking and pitting corrosion) compared to austenitic stainless steels [3,4]. For this reason, duplex stainless steels, like other stainless steels, are widely used in nuclear facilities, oil and natural gas pipelines (including undersea pipes), offshore platforms, the paper industry, purification facilities, chemical facilities, and maritime (shipbuilding) areas [5-19]. In many of these applications, welding of duplex stainless steel is inevitable.

The weldability of duplex stainless steels is generally better than ferritic stainless steels but worse than austenitic stainless steels. Weld seams of these alloys provide the desired level of mechanical strength and corrosion resistance in most applications, even without being subjected to any heat treatment. The weld nugget microstructure is completely ferritic when it solidifies, but during cooling, some of the ferrite transforms into austenite and the microstructure of the weld nugget becomes duplex. To ensure adequate austenite formation in the heat-affected zone (HAZ), rapid cooling should be avoided. The high heat input and subsequent rapid cooling during the welding process can cause microstructural changes and/or precipitations that negatively affect the properties of the weld seam. Important factors affecting the cooling rate are heat input, minimum and maximum welding parameters specified in the welding procedure, and preheat and interpass temperatures. In a normal welding application, it is

difficult for 475°C brittleness to occur as sigma (σ) phase formation temperatures are passed quickly.

The heat the material is exposed to during the welding process can change the ferrite and austenite ratio of the weld metal and HAZ. The change in this ratio causes the mechanical properties and corrosion resistance of the material to diminish. Therefore, the welding method, welding procedure, and filler wire must be selected to balance this ratio and prevent the formation of harmful phases such as nitrides, carbides, and intermetallics [20]. For example; nitrogen (N) is added to the base material to ensure the easy formation of austenite in the HAZ region adjacent to the fusion zone which is subjected to high temperatures. In addition, to increase the austenite that provides the necessary ductility and toughness in the weld metal, filler wires containing 2-3% more Ni than the Ni content of the base metal are used [21]. It is preferred to use duplex stainless steel filler wire such as ER2209 when welding duplex stainless steels and welding these steels with austenitic stainless steels and carbon or low alloy steels. In some applications, austenitic stainless steel filler wires such as 309L and 309LMo may be recommended, but these lead to a decrease in N content and an increase in the ferritic structure in the HAZ exposed to high temperatures [22]. As in structural steels and other stainless steels [7-18], the most commonly used welding methods in the joining of duplex stainless steels are shielded metal arc welding (SMAW), gas metal arc welding (GMAW), gas tungsten arc welding (GTAW), submerged arc welding (SAW), and flux-cored wire arc welding (FCAW) methods. These high arc energy methods lead to more austenite formation in the weld seam due to the lower cooling rates in these methods [23,24]. On the other hand, high energy density and therefore lower heat input plasma arc welding (PAW), laser beam welding (LBW), and electron beam welding (EBW) methods are also used in the welding of these steels [25-28]. However, lower amounts of austenite form in the weld nugget in these methods as a result of higher cooling rates involved [29,30]. In addition, intensive studies have recently been carried out on the use of new and advanced welding technologies to join duplex steels using appropriate additional wire and welding parameters. Among these, friction stir welding (FSW) [30-40], which was developed to join low melting point metals and alloys such as Al-alloys, active flux gas tungsten arc welding (A-TIG) and hybrid welding techniques (such as hybrid plasma arc-GMAW, hybrid plasma arc-GTAW, hybrid laser-GMAW, and hybrid laser-GTAW) have been investigated [13,23,42-52].

Heat input significantly affects the changes in the microstructure (austenite-ferrite balance) in the weld zone of duplex stainless steel welded joints. In general, a heat input between 0.5-2.0 kJ/mm is recommended to obtain appropriate austenite and ferrite ratios in these steels and to control harmful intermetallic phases [53]. In fact, Hertzman [54] reported that the strength of SAF 2205 duplex stainless steel connections did not change significantly when a heat input of 0.3–2.0 kJ/mm was used or when the amount of ferrite in the weld seam was between 23-53%. Additionally, heat input has a significant impact on the nugget form and the metallurgical, mechanical, and corrosion properties of the welded joint [46]. Therefore, the cooling rate, which varies depending on the heat input and welding method, also plays an important role in the grain size and phase formation in the weld zone [55]. As is clear from the literature, low heat input and rapid cooling lead to the formation of harmful Cr_2N and CrN phases, so they should be avoided.

The GTAW method is one of the most popular welding methods for welding duplex stainless steel. However, the low efficiency of this method limits its widespread use [21,56-59]. For example, Zhang et al. [56] joined 14 mm thick UNS S31803 duplex stainless-steel plates with GTAW and flux-cored wire arc welding (FCAW) using two different shielding gases, pure argon, and argon with 2% nitrogen content and compared the results. A microstructure consisting of ferrite phase, grain boundary austenite, and Widmanstatten austenite was formed in the weld seam of the joints obtained by the GTAW method using both pure argon and nitrogen-doped argon shielding gas. However, the ferrite phase is much less in the weld seam obtained with nitrogen-doped shielding gas. On the other hand, a microstructure containing ferrite phase, intragranular austenite, and grain boundary austenite was formed in the weld nugget of the joints produced by flux-cored wire arc welding. In addition to these phases, inclusions were also detected in the weld zone. Additionally, it has been reported that the addition of nitrogen to the shielding gas in the GTAW process increases the toughness and that joints obtained with flux-cored wire show lower toughness in both the HAZ and the fusion zone. It is also worth pointing out that it is a well-known phenomenon that the formation of the Widmanstatten ferrite in the weld region of structural steels reduces the impact strength [58,59].

Low heat input welding methods (e.g., EBW, PAW, and LBW) offer many advantages in fusion joining of duplex stainless steels, as in all metallic materials, such as low distortion and residual stress formation, very narrow HAZ formation or no significant HAZ formation, high welding speeds, the possibility of welding thick plates, and high efficiency. However, since these methods inherently lead to high cooling rates, this causes excessive ferrite formation in the weld seam as there is not enough time for the solidified ferrite phase to transform into austenite, thus deteriorating the austenite-ferrite balance [28,60-64]. This necessitates heat treatment to ensure ferrite/austenite balance in the fusion zone after welding. Another way to partially preserve the ferrite-austenite balance in the weld region is to use pure nitrogen shielding gas instead of argon shielding gas in the laser

welding process [64]. In addition, since vacuum is used in electron welding, nitrogen loss also occurs, and this negatively affects corrosion resistance as well as mechanical properties [28]. Both high energy density methods such as LBW and EBW and hybrid welding applications are not widely used methods in welding duplex stainless steels. Additionally, these methods require large investment costs. Similarly, the solid-state FSW process, which provides successful results in low-melting alloys such as Al-alloys, also has some disadvantages. This method requires high-cost stirring tools resistant to high temperatures and tight fixing of the plates to be welded before welding and has geometric limitations. Additionally, low cooling rates may lead to negative changes in the microstructure. Additionally, welding speeds in this method are lower than traditional fusion welding processes.

Another method that can be used for welding thick sheets is the active flux GTAW (A-TIG) method. With this method, deep penetration welds can also be obtained in duplex stainless steels. For example, in their study, Zou et al. [49] successfully joined SUS329J4L duplex stainless-steel plates with relatively low heat input A-TIG welding. It has been reported that the microstructure in the fusion zone consists of the ferrite phase, grain boundary austenite (intergranular austenite), and austenite formed within the grains (intragranular austenite). However, this method is not a commonly used welding method for welding duplex stainless steel plates. Additionally, Ravichandran et al. [65] used S/N ratio and ANOVA techniques to determine the optimum welding parameters (such as current, gas flow rate, and welding speed) for welding duplex stainless steels with the GTAW method. S/N analysis results reported that the highest impact resistance and hardness values were obtained at 150 A current, 14 L/min gas flow rate, and 210 mm/min welding speed. Naik and Reddy [66] also TIG welded 6 mm thick 2205 duplex stainless steel plates using ER316 wire and reported that the best results were obtained with a current of 250 A.

As can be understood from the above discussion, there is a need for a detailed understanding of issues such as the effect of heat input in the welding of these steels with low-cost conventional arc welding methods and the development of reliable conventional welding procedures for joining these steels. Therefore, in this study, 3 mm thick SAF 2205 duplex stainless steel plates were butt-welded using a 2 mm diameter ER2209 duplex filler wire in 2 passes with the GTAW method using different heat inputs. To characterize the microstructures formed in the weld region of the fabricated welded joints, detailed microstructural examinations and microhardness measurements were carried out using an optical microscope on the metallography samples cut from the welded joints. Samples extracted from both the base material and the welded joints were subjected to tensile testing to determine the mechanical properties and welding performance. In addition, the effects of heat input on the microstructural changes in the weld region and the performance of the welded joints under tensile and bending conditions were examined.

2. Materials and Methods

In this study, the weldability of 3 mm thick cold-rolled AISI 318LN type duplex stainless steel (SAF 2205 - material number 1.4462) plates with the GTAW method and the effect of heat input on the welding performance were investigated. The chemical compositions of the plates and filler wire used are given in Table 1.

Table 1. Compositions of base plate and filler wire (wt.%)

Chemical composition (wt. %)								
Material	C	Si	Mn	Cr	Ni	Mo	Cu	N
BM*	0,016	0,37	1,49	22,2	5,7	3,1	0,25	0,185
Filler wire	0,01	0,45	1,45	23,0	8,5	--	--	0,15

*In addition, BM also contains % 0,017 Nb, % 0, 18 Co, % 0,026 P, and % 0,001 S.

For welding experiments, rectangular pieces 195x300 mm in size were cut from the commercially available plate perpendicular to the rolling direction, and the weld grooves were machined in these parts as shown in Figure 1. The surfaces were mechanically cleaned with a stainless-steel brush before the joining process. Welding trials were carried out in two passes, namely root pass and filler pass, using a 2 mm diameter duplex filler wire (ER2209) at different heat inputs. During the welding process, filler wire was fed at a speed of 1.5 mm/s in each pass. In all welding experiments, 99.95% purity argon gas was supplied to the welding area as a protective gas at a flow rate of 16 L/min. In all welds, a ceramic backing was used to prevent underfill failure as a result of liquid metal flowing from the weld base. Additionally, the chassis connection and extension cable were kept in a straight position during the welding process. Other welding parameters used in the welding process are given in Table 2.

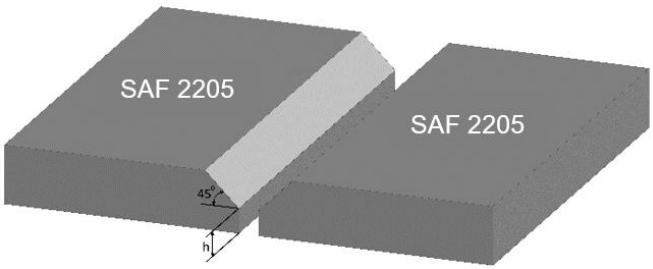

Figure 1. Preparation of plates for welding (h: 1 mm, the gap between the plates at weld root: 2 mm).

One metallography sample, two bending samples, and four tensile samples were extracted from each welded joint obtained to determine the microstructural changes occurring in

the weld region and to evaluate the effect of the changes in the microstructure on the mechanical properties. For comparison purposes and to evaluate joint performance, at least three tensile specimens were also prepared from the base plate according to ASTM A370 standards. To examine the weld cross-section following grinding and polishing, metallography samples were etched for 20 seconds using a solution consisting of 50 ml HCl and 150 ml HNO3 (aqua regia). In addition to microhardness measurements, detailed microstructure examinations were also carried out on the metallography samples. As shown schematically in Figure 2, microhardness measurements were made on the metallography samples on a line around the centre of the weld cross-section, using a load of 980 N (10 kg) in all regions in the samples, namely in the base plates, HAZs, and FZs. With these measurement values, the hardness distribution (hardness profile) along the weld cross-section was determined for each welded joint.

Table 2. Weld parameters used in welding trials.

Welding Procedure	Current (A)	Voltage (V)	Weld Speed (mm/min)	Heat Input (kJ/mm)
Low Heat Input*	120	28	36	3,92
Medium Heat Input*	130	28	36	4,25
High Heat Input*	140	28	36	4,57

Heat input was calculated using the following equation: $q = \eta I U 60/1000 v$ (q = heat input (kJ/mm), η = arc efficiency (for GTAW it is 0,7), U = arc voltage (V), I = current (A), and v = weld speed (mm/min)).

Additionally, to determine the mechanical properties, mechanical performances, and joint qualities of welded plates, tensile test specimens extracted from both the base plate and welded joints were tested with a deformation rate of 0.0025 1/s according to ISO 6892-1. Two bending samples were also extracted from each welded joint to determine whether there was any cracking under bending conditions in the weld region of the joints produced. One of these bending specimens was bent in the face-bending condition and the other in the root-bending configuration. The bending samples were bent to approximately 140-150 degrees with the weld centre in the middle position.

3. Results and Discussion

The findings obtained in this study will be discussed under two subheadings in this section.

3.1. Microstructural Aspects

The microstructure of the 3 mm thick SAF 2205 duplex stainless steel base plate used in this study is given in Figure 3. As can be seen from the figure, the base plate has a microstructure consisting of austenite (50%) and delta ferrite (50%). Owing to the ferrite/austenite balance in this microstructure, these steels exhibit high mechanical properties and at the same time superior corrosion resistance (higher resistance to stress corrosion cracking and pitting corrosion) compared to austenitic stainless steels.

Duplex stainless steels solidify completely in ferritic mode, and austenite solid nuclei are formed in the ferrite phase under the ferrite solidification curve (the solidification sequence is as follows: Liquid → Liquid + δ → δ + γ), resulting in a microstructure consisting of ferrite and austenite. This solidification mode depends on the Cr_{eq}/Ni_{eq} ratio and can be better understood from the Fe-Cr-Ni phase diagram given in Figure 4, which is a very good reference for understanding the solidification mode [56,67,68].

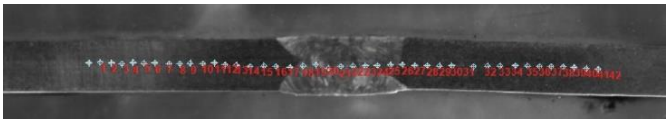

Figure 2. Macrograph showing the points where microhardness measurements were made in the weld cross-section.

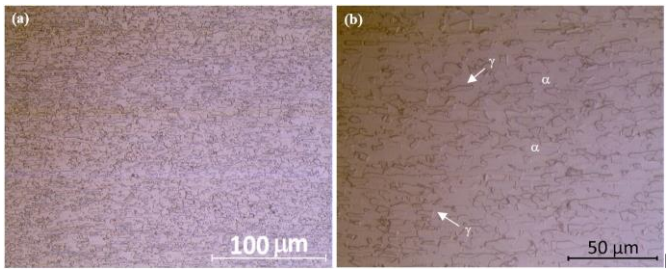

Figure 3. Microstructure of the duplex stainless steel base plate used in the study: (a) 200X and (b) 500X magnification.

The composition of typical duplex stainless steels corresponds to the α + γ phase region. Duplex stainless steels such as SAF 2205 and SAF 2507 are marked in Figure 4. As can be seen from this figure, the ferrite phase is constantly present from solidification down to room temperature, and therefore, although it is delta (δ) ferrite, it is called alpha (α) ferrite because it transforms with the same chemical composition [69].

In practice, duplex stainless steels are resistant to solidification cracking because they contain low impurity. If the Cr_{eq}/Ni_{eq} ratio is greater than 1.95, the solidification in stainless steels is completely ferritic. However, if this ratio is between 2.25-3.5 (for SAF 2205, this ratio is 2.62), the solidification is two-phase (ferrite + austenite). In general, a microstructure consisting of a ferrite matrix containing grain boundary austenite (GBA) nucleated within the ferrite matrix and Widmanstatten austenite (WA) is observed in the fusion zone of duplex stainless steels [70]. Later, with the effect of the

cooling rate, an intragranular austenite phase (IGA) is also formed, which requires more driving force at lower temperatures and is sensitive to pitting corrosion.

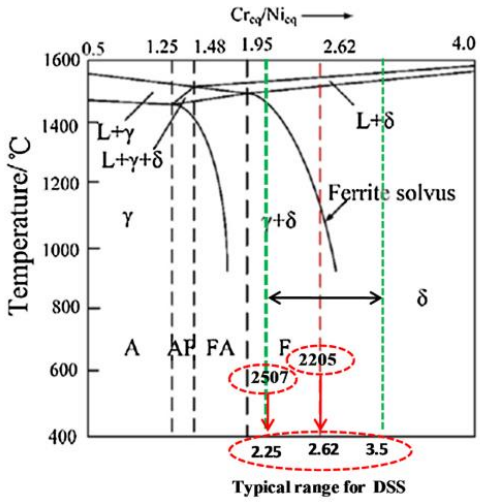

Figure 4. Fe-Cr-Ni diagram showing the types of solidification occurring in stainless steels depending on the Cr_{eq}/Ni_{eq} ratio (solidification of SAF 2205 duplex stainless steel is also marked in the diagram).

Figure 5 gives macrographs showing the weld cross-sections of the welded joints obtained in this study. As can be seen from these macrographs, the weld profiles of the joints are quite good and no weld defects such as porosity, cracks, etc. were observed in the weld regions, except the low heat input joint. This indicates that the joint quality of the welded plates is satisfactory. However, a decrease in cross-section was observed in the joint obtained with low heat input as a result of insufficient filling. The microstructure formed in the fusion zone of the joint produced with low heat input (3.92 kJ/mm) is shown in Figure 6. As can be seen from the figure, the microstructure contains a ferrite phase containing grain boundary austenite, a small amount of Widmanstatten austenite, and intragranular austenite. Additionally, another noteworthy point is that the amount of ferrite in the fusion zone of this joint is higher than the austenite content.

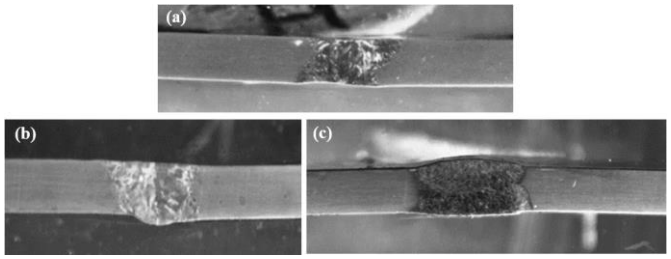

Figure 5. Macrographs showing the cross-section of the welded joints: The welded joint produced with a heat input of: (a) 3.92, (b) 4.25 and (c) 4.57 kJ/mm. (thickness: 3mm).

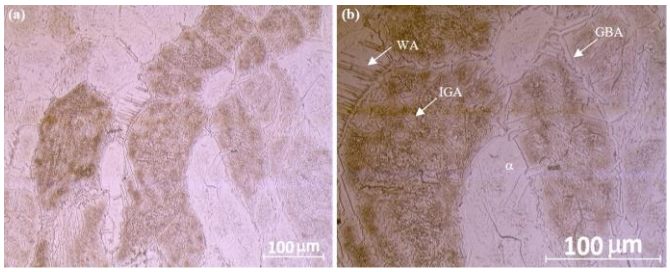

Figure 6. Microstructure in the FZ of low-heat input joint (3.92 kJ/mm): (a) X100 and (b) X200 magnification. (GBA: Grain boundary austenite, IGA: Intragranular austenite and WA: Widmanstten austenite).

As an example of the fusion zone microstructures of joints made with medium (4.25 kJ/mm) and high (4.57 kJ/mm) heat inputs, the microstructure observed in the fusion zone of the joint with high-heat input is given in Figure 7. As can be seen from the figure, the fusion zone microstructure of these joints comprises a ferrite phase containing grain boundary austenite, a small amount of Widmanstatten austenite, and intragranular austenite, similar to the joint produced with low heat input. However, the amount of Widmanstatten austenite and intragranular austenite is higher. In addition, while a finer-grained equiaxed structure forms in the fusion zone of the joint produced with low heat input, it is observed that a coarse-grained, columnar grain structure forms in the fusion of the joints obtained with medium and high heat inputs. This columnar grain structure is more evident in the joint made with high heat input (4.57 kJ/mm) (Figure 7b). In addition, in the fusion zones of joints produced with medium and high heat input, especially in that of the high-heat input, the amount of austenite is much higher than in the low-heat input joint, and the ferrite-austenite balance is better.

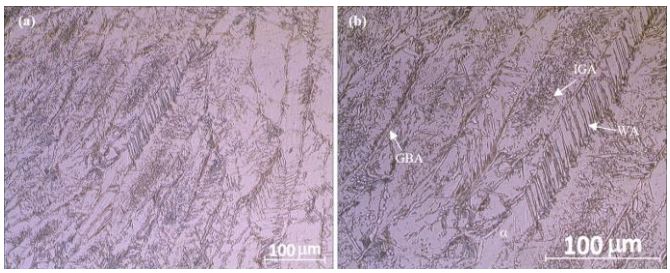

Figure 7. Microstructure in the FZ of high-heat input joint (4,57 kJ/mm): (a) X100 and (b) X200 magnification. (GBA: Grain boundary austenite, IGA: Intragranular austenite and WA: Widmanstten austenite).

As an example of welded joints produced with 3.92 and 4.25 kJ/mm heat inputs, optical micrographs showing the microstructure of the heat-affected zone (HAZ) of the joint produced with medium-heat input (4.25 kJ/mm) are given in Figure 8. As can be seen from the figure, no visible HAZ was present in both joints. On the other hand, it was observed that an evident HAZ occurred in the welded joint obtained with high heat input (4.57 kJ/mm). As clearly seen from Figure 9,

recrystallization took place in the HAZ of this joint. The temperatures reached during welding in this region are at a level that will lead to the formation of the ferrite phase. Therefore, as a result of the recrystallization in the HAZ of this joint, a relatively coarse-grained ferritic structure was formed due to the relatively high heat input. Moreover, due to the relatively rapid cooling after welding, the formation of the austenite phase within the ferrite phase was limited. As a result, the microstructure in the HAZ of this joint consists of coarse ferrite grains and a small amount of grain boundary austenite and intragranular austenite (austenite phase formed within the grains). In addition, the ferrite phase present in the microstructure is more than the austenite phase, due to the relatively rapid cooling after welding and thus the limited formation of the austenite phase within the ferrite phase.

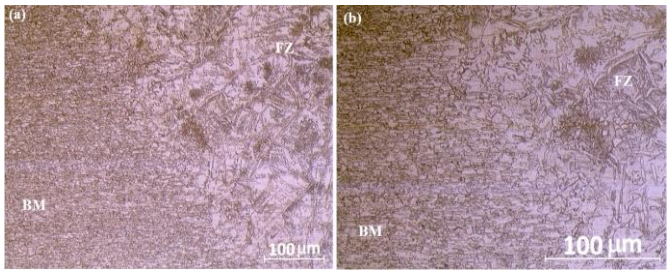

Figure 8. Microstructure in the HAZ of medium-heat input joint (4,25 kJ/mm): (a) X100 and (b) X200 magnification. (BM: Base metal and FZ: Fuzion zone).

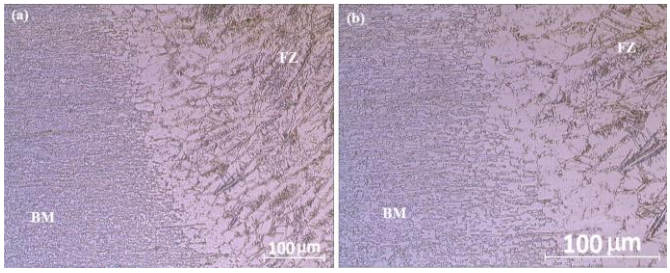

Figure 9. Microstructure in the HAZ of high-heat input joint (4,57 kJ/mm): (a) X100 and (b) X200 magnification. (BM: Base metal and FZ: Fuzion zone).

3.2. Mechanical Properties

3.2.1. Microhardness

The hardness profiles showing the hardness distribution along the weld cross-sections of all the joints drawn using the hardness values obtained by microhardness measurements taken at the points shown in Figure 2 are given in Figure 10. As seen from the figure, the hardness profile of the low-heat input joint (3.92 kJ/mm), which exhibited an increase in hardness in the weld region, is different from those of the other joints (medium and high heat inputs). This indicates that the ferrite-austenite ratio in the fusion zone of this joint is negatively affected and is related to the increase in the amount of ferrite as a result of less austenite formation due to rapid cooling. These results are in good agreement with the microstructural observations.

On the other hand, no hardness increase was observed in the weld regions of the joints produced using medium and high heat inputs (4.25 and 4.57 kJ/mm), and hardness values similar to the hardness value of the base material were measured. Therefore, while the low-heat input joint displayed an increase in strength (strength overmatching) in the weld region, the joints produced with medium and high heat inputs exhibited a homogeneous hardness distribution throughout the weld cross-section (strength even matching weld region). These results are due to the preservation of the ferrite-austenite balance in these two joints, especially in the high-heat input joint, and are compatible with the microstructural investigations. In addition, although coarse ferrite grains and grain boundary austenite are formed in the very narrow HAZ exposed to high heat adjacent to the fusion line of the high heat input joint, no change variation (hardness decrease) in the hardness profile was observed. This is attributed to the fact that this region is very narrow and as a result, no hardness measurement could be made in this region.

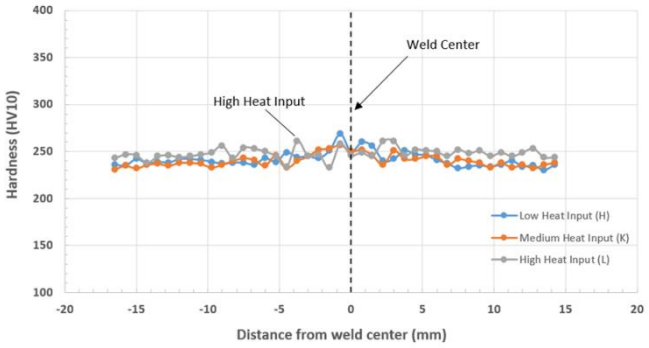

Figure 10. Hardness profiles of the joints obtained with different heat inputs.

3.2.2. Tensile and Bending Performance

The tensile test results obtained from the base plate samples and the samples extracted from the joints perpendicular to the weld line are summarized in Table 3. As can be seen in Figure 11, all the specimens extracted from the low-heat input joint fractured within the weld region. On the other hand, two of the tensile samples of the medium-heat input joint broke within the FZ and the other two failed within the base plate at a certain distance from the HAZ. While only one of the samples of the high-heat input joint broke off from the weld region, the other three samples fractured in the base metal close to the HAZ. These results are also compatible with the microstructural examinations. It is caused by the deterioration of the ferrite-austenite phase balance in the FZ of the low-heat input joint along with a significant thinning in the weld cross-section in this joint due to insufficient filling, as seen from the macrograph of this joint in Fig. 5(a). Additionally, as seen from the table, the tensile strength of the samples of the low-

heat input joint is lower those that of base plate samples, and the joint performance value in terms of strength is 96%. The strength levels of medium and high-heat input joint samples, particularly that of high-heat input joint, are higher than those of the low-heat input joint and the base plate samples, thus the strength performance is around 102%. This situation is clearly seen from the stress-strain curves obtained from the base plate and welded joint samples given in Figure 12. The reason why the high-heat input joint exhibits high strength performance is the result of better preservation of the ferrite-austenite balance in the fusion zone of this joint (Figure 7b).

Table 3. Tensile test results (average values are given in parentheses).

Specimen	R_m (MPa)	Elongation (%)	Strength Performance (%)	Ductility Performance (%)
Base Metal	807; 811; 809; 806 (**808**)	26; 26; 26; 25 (**26**)	--	--
Low Heat Input Joint	757; 760; 777; 799 (**773**)	9; 7; 9; 13 (**10**)	96	38
Medium Heat Input Joint	826; 821; 745; 759 (**788**)	22; 22; 7; 9 (**15**)	98	58
High Heat Input Joint	833; 831; 816; 831 (**828**)	25; 21; 22; 23 (**23**)	102	88

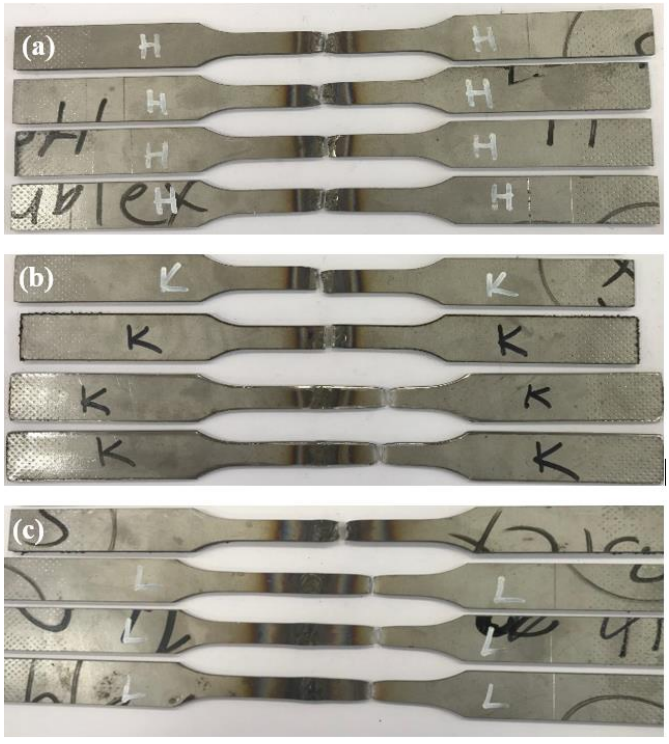

Figure 11. Fracture locations in tensile samples of the welded joints: (a) Low, (b) medium, and (c) high heat input joints.

On the other hand, as seen in Table 3, the elongation values of the welded joint samples are significantly lower than the base plate. This is due to the inhomogeneity of the welded joint samples. This situation is especially evident in the low-heat input joint, and the joint performance in terms of ductility is quite low (38%). The reason for this is that in these samples, where the fracture occurs in the FZ, no elongation occurs in the base plate, and therefore plastic deformation is limited to the weld region (i.e., confined plasticity). The highest ductility performance was displayed by the high-heat input joint (i.e., 88%). This result is consistent with the fact that all but one of the samples broke from the base plate due to better preservation of the ferrite-austenite balance in the FZ of this joint. Similar results are also observed in welded joints with a strength increase in the weld area (strength overmatching joints) [71-74]. Moreover, generally, much lower ductility performance values have been reported in high-strength Al-alloy welded joints with excessive strength loss in the weld region (highly strength undermatching joints) where only the weld region undergoes plastic deformation [75-80] as well as in diffusion welded dissimilar joints in which plastic deformation occurs only in the half of the sample [81,82].

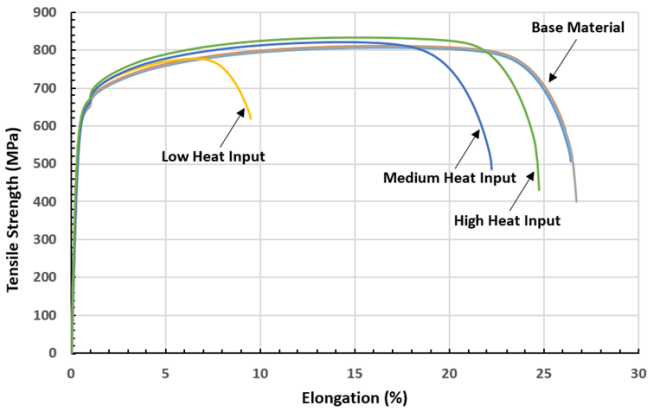

Figure 12. Stress-strain curves obtained from the base plate and welded samples.

In addition, no cracking was observed in any of the samples in both the surface bending and root bending tests performed on all welded joints, indicating that the weld quality was satisfactory. These results are compatible with microstructural observations in which discontinuities such as cracks and porosity are not detected in the weld regions of the joints.

4. Conclusion

In this study, 3 mm thick cold-rolled SAF 2205 duplex stainless steel plates were successfully welded in two passes by the GTAW method using an ER 2209 filler wire with a diameter of 2 mm. The results obtained from this study can be summarized as follows:

- No weld discontinuities such as porosity or crack formation were detected in all the welded joints produced.

- A microstructure comprising of ferrite phase containing grain boundary austenite, a small amount of Widmanstatten austenite, and intragranular austenite was detected in the FZ of the welded joints. While an equiaxed structure was formed in the FZ of the low-heat input joint, coarse columnar grains were observed in the FZ of the medium and high-heat input joints. In addition, the amount of austenite in the FZ was higher in medium and high-heat input joints, especially in the high-heat input joint.
- While no visible HAZ was observed in the low and medium heat-input joint, a distinct HAZ occurred as a result of recrystallization in the high-heat input joint.
- The hardness profile of the low-heat input joint (3.92 kJ/mm) is different from the other joints (medium and high-heat inputs), and an increase in hardness is observed in the weld region of this joint, while the medium and high-heat input joints (4.25 and 4.57 kJ/mm) mm) exhibited a more homogeneous hardness distribution across the weld cross-section.
- All transverse tensile test specimens of the low-heat input joint broke off within the weld region. On the other hand, two of the samples of the medium-heat input joint and only one of the samples of the high-heat input joint fractured within the weld nugget, the other samples failed in the base plate.
- The high-heat input joint showed the highest strength performance value (i.e., 102%). This is the result of better preservation of the ferrite-austenite balance in the FZ of this joint. On the other hand, due to the non-homogeneity of the transverse tensile samples, the ductility performance of all joints is low, and the highest ductility performance (i.e., 88%) was displayed by the high-heat input joint. This indicates that heat input plays an important role on the microstructural evolution in the FZ and thus mechanical performance. Sufficiently higher heat inputs for avoiding fast cooling after the welding give better results.
- No cracking occurred in both the surface and root bending samples extracted from all joints. This shows that the heat input range used in the study does not have a significant effect on the joint performance under bending conditions.

Declaration of Competing Interest

The authors declare that they have no known competing financial interests or personal relationships that could have appeared to influence the work reported in this paper.

Acknowledgement

The authors also thank Mr. Sedat UYSAL (Managing Director) and Mr. Tuğrul YAZGAN (Quality and Mechanical Laboratory Supervisor) as well as Mr. Erhan Zeytun and Mr. Ferhat Gürler (Mechanical Laboratory Personnel) from NOKSEL Steel Pipe Inc., İskenderun-Hatay, Turkey, for their valuable support in conducting the metallographic investigations and mechanical tests (tensile and bending tests).

References

[1] T. Oshima, Y. Habara, and K. Kuroda, Efforts to save nickel in austenitic stainless steels, ISIJ Int., 47 (2007) 359-364.

[2] P. Boillot and J. Peultier, Use of stainless steels in the industry: recent and future developments, Procedia Eng., 83 (2014) 309-321.

[3] S.K. Ghosh and S. Mondal, High temperature ageing behaviour of a duplex stainless steel, Mater. Charact., 59 (2008) 1776-1783.

[4] B. Gideon, L. Ward, and G. Biddle, Duplex stainless steel welds and their susceptibility to intergranular corrosion, J. Miner. Mater. Charact. Eng., 7(3)(2008) 247-263.

[5] J. Verma and R.V. Taiwade, Dissimilar welding behavior of 22% Cr series stainless steel with 316L and its corrosion resistance in modified aggressive environment, J. Manuf. Process., 24 (2016) 1-10.

[6] K.D. Ramkumar et al., Studies on the structure–property relationships and corrosion behaviour of the activated flux TIG welding of UNS S32750, J. Manuf. Process., 23 (2016) 231-241.

[7] M. Şenol and G. Çam, Investigation into microstructures and properties of AISI 430 ferritic steel butt joints fabricated by GMAW, Int. J. Press. Ves. Pip., 202 (2023) 104926.

[8] A. Günen et al., A new approach to improve some properties of wire arc additively manufactured stainless steel components: Simultaneous homogenization and boriding, Surface & Coating Technology, 460 (2023) 129395.

[9] U. Gürol et al., Effect of powder-pack aluminizing on microstructure and oxidation resistance of wire arc additively manufactured stainless steels, Surf. Coat. Technol., 468 (2023) 129742.

[10] H.T. Serindağ and G. Çam, Characterizations of microstructure and properties of dissimilar AISI 316L/9Ni low alloy cryogenic steel joints fabricated by GTAW, J. Mater. Eng. Perform., 32 (2023) 7039-7049.

[11] H.T. Serindağ and G. Çam, Multi-pass butt welding of thick AISI 316L plates by gas tungsten arc welding: Microstructural and mechanical characterization, Int. J. Press. Ves. Pip., 200 (2022) 104842.

[12] M. Ezer and G. Çam, A Study on microstructure and mechanical performance of gas metal arc welded AISI 304L joints, Materialwissenschaft und Werkstofftechnik, 53 (9) (2022) 1043-1052.

[13] T. Küçükömeroğlu et al., Investigation of mechanical and microstructural properties of friction stir welded dual phase (DP) steel, IOP Conf. Series: Mater. Sci. Eng., 629 (2019) 012010.

[14] H.T. Serindağ and G. Çam, Microstructural and mechanical characterization of gas tungsten arc welded 10 mm thick AISI 316L joints, Düzce University Journal of Science & Technology, 10 (4) (2022) 1873-1889.

[15] H.T. Serindağ and G. Çam, Microstructure and mechanical properties of gas metal arc welded AISI 430/AISI 304 dissimilar stainless steels butt joints, Journal of Physics: Conference Series, 1777 (2021) 012047.

[16] M. Şenol and G. Cam, Microstructural and mechanical characterization of gas metal arc welded AISI 430 ferritic stainless steel joints, European J. Eng. and Natural Sciences (EJENS), 5 (1) (2020) 52-60.

[17] M. Ezer and G. Çam, Investigation of the microstructure and mechanical properties of gas metal arc welded AISI 304 austenitic stainless steel butt joints, European J. Eng. and Natural Sciences (EJENS), 5 (1) (2020) 43-51.

[18] J.C. Lippold and D.J. Kotecki, 'Welding metallurgy and weldability of stainless steels', John Wiley and Sons, Inc., Hoboken, NJ, USA, (2005) 141-200.

[19] G. Çam, 'Kaynak Bilimi ve Teknolojisi', Nobel Akademik Yayıncılık, Ankara, (2020) 205-209.

[20] L. Karlsson, Welding duplex stainless steels - A review of current recommendations, Weld. World, 56 (2012) 65-76.

[21] S. Geng et al., Evolution of microstructure and corrosion behavior in 2205 duplex stainless steel GTA-welding joint, J. Manuf. Process., 19 (2015) 32-37.

[22] H. Dolutaş and M. Cavcar, 'Dupleks Paslanmaz Çeliklerin Kaynağı', Oerlikon Kaynak Elektrodları ve Sanayi A.Ş., Ankara, (2001) 7-11.

[23] J. Verma and R.V. Taiwade, Effect of welding processes and conditions on the microstructure, mechanical properties and corrosion resistance of duplex stainless steel weldments - A review, J. Manuf. Process., 25 (2017) 134-152.

[24] S.H. Wang et al., Gamma phase transformation in pulsed GTAW weld metal of duplex stainless steel, Mater. Sci. Eng. A, 420 (2006) 26-33.

[25] A.-H.I. Mourad, A. Khourshid, and T. Sharef, Gas tungsten arc and laser beam welding processes effects on duplex stainless steel 2205 properties, Mater. Sci. Eng. A, 549 (2012) 105-113.

[26] E. Taban and E. Kaluc, Welding behaviour of duplex and super-duplex stainless steels using laser and plasma arc welding processes, Weld. World, 55 (2011) 48-57.

[27] S. Krasnorutskyi, D. Keil, S. Schmigalla, M. Zinke, A. Heyn, and H. Pries, Metallurgical investigations on electron beam welded duplex stainless steels, Weld. World, 56 (2012) 34-40.

[28] J.S. Ku, N.J. Ho, and S.C. Tjong, Properties of electron beam welded SAF 2205 duplex stainless steel, J. Mater. Process. Technol., 63 (1997) 770-775.

[29] T. Kannan and N. Murugan, Effect of flux cored arc welding process parameters on duplex stainless steel clad quality, J. Mater. Process. Technol., 176 (2006) 230-239.

[30] J. Nowacki, Ferritic-austenitic steel and its weldability in large size constructions, J. Achiev. Mater. Manuf. Eng., 32 (2) (2009) 115-141.

[31] M.M.Z. Ahmed, et al., Friction stir welding in the aerospace industry: The current progress and state-of-the-art review, Materials, 16 (2023) 2971.

[32] G. Çam, V. Javaheri, and A. Heidarzadeh, Advances in FSW and FSSW of dissimilar Al-alloy plates, Journal of Adhesion Science and Technology, 37 (2) (2023) 162-194.

[33] N. Kashaev, V. Ventzke, and G. Çam G, Prospects of laser beam welding and friction stir welding processes for aluminum airframe structural applications, J. Manuf. Process., 36 (2018) 571-600.

[34] G. Çam and G. İpekoğlu, Recent developments in joining of aluminium alloys, Int. J. Adv. Manuf. Technol., 91 (5-8) (2017) 1851-1866.

[35] G. İpekoğlu et al., Investigation into the effect of temper condition on friction stir weldability of AA6061 Al-alloy plates, Kovove Mater., 51 (3) (2013) 155-163.

[36] G. Çam, Friction stir welded structural materials: Beyond Al-alloys, Int. Mater. Rev., 56 (1) (2011) 1-48.

[37] G. İpekoğlu, Ö. Akçam, and G. Çam, Determination of the suitable weld parameters for friction stir welding of AA6061-T6 plates with different thicknesses, Afyon Kocatepe Univ. J. of Sci. and Eng., 18 (1) (2018) 324-335.

[38] G. Çam, Friction stir welding: A novel welding technique developed for Al-alloys, Mühendis ve Makine, 46 (541) (2005) 30-39.

[39] M.M.Z. Ahmed, et al., A review on friction stir welding of dissimilar Al- and Mg-alloys: Scientometric analysis and strategies for achieving high-quality joints, Journal of Magnesium and Alloys, 11 (2023) 4082-4127.

[40] U.A. Khaliq, et al., A comprehensive review on friction stir welding of aluminum with magnesium: A new insight on joining mechanisms by interfacial enhancement, Journal of Materials Research and Technology (JMR&T), 27 (2023) 4595-4624.

[41] A. Günen et al., Microstructural and mechanical properties of friction stir welded pure lead, Indian J. of Eng. & Mater. Sciences, 25 (1) (2018) 26-32.

[42] H.S. Wang, Effect of welding variables on cooling rate and pitting corrosion resistance in super duplex stainless weldments, Mater Trans., 46 (2005) 593-601.

[43] M.C. Theodoro et al., Dissimilar friction stir welding between UNS S31603 austenitic stainless steel and UNS S32750 superduplex stainless steel, Metall. Mater. Trans. B, 46 (2015) 1440-1447.

[44] T. Saeid et al., Effect of friction stir welding speed on the microstructure and mechanical properties of a duplex stainless steel, Mater. Sci. Eng. A, 496 (2008) 262-268.

[45] R.I. Hsieh, H.Y. Liou, and Y.T. Pan, Effects of cooling time and alloying elements on the microstructure of the gleeble-simulated heat-affected zone of 22% Cr duplex stainless Steels, J. Mater. Eng. Perform., 10 (2001) 526-536.

[46] P.K. Giridharan and N. Murugan, Optimization of pulsed GTA welding process parameters for the welding of AISI 304L stainless steel sheets, Int. J. Adv. Manuf. Technol., 40 (2009) 478-489.

[47] K. Nanda Naik et al., Finite element simulation of A-TIG welding of duplex stainless steel 2205 using SYSWELD, Appl. Mech. Mater., 592-594 (2014) 374-379.

[48] A. Berthier, P. Paillard, and F. Christien, Structural and chemical evolution of super duplex stainless steel on activated tungsten inert gas welding process, Sci. Technol. Weld. Join., 14 (2009) 681-690.

[49] Y. Zou, R. Ueji, and H. Fujii, Mechanical properties of advanced active-TIG welded duplex stainless steel and ferrite steel, Mater. Sci. Eng. A, 620 (2015) 140-148.

[50] E.M. Westin, K. Stelling, and A. Gumenyuk, Single-pass laser-GMA hybrid welding of 13.5 mm thick duplex stainless steel, Weld. World, 55 (2011) 39-49.

[51] E. Taban, Joining of duplex stainless steel by plasma arc, TIG, and plasma Arc + TIG welding processes, Mater. Manuf. Process., 23 (2008) 871-878.

[52] K. Yurtisik et al., Characterization of duplex stainless steel weld metals obtained by hybrid plasma-gas metal arc welding, Soldag Insp., 18 (2013) 207-216.

[53] M. Sadeghian et al., Effect of heat input on microstructure and mechanical properties of dissimilar joints between super duplex stainless steel and high strength low alloy steel, Mater. Des., 60 (2014) 678-684.

[54] S. Hertzman, The influence of nitrogen on microstructure and properties of highly alloyed stainless steel welds, ISIJ Int., 41 (6) (2001) 580-589.

[55] N. Karunakaran, Effect of pulsed current on temperature distribution, weld bead profiles and characteristics of GTA welded stainless steel joints, Int. J. Eng. Technol., 2 (2012) 908-1916.

[56] Z. Zhang et al., Investigation on microstructure evolution and properties of duplex stainless steel joint multi-pass welded by using different methods, Mater. Des., 109 (2016) 670-685.

[57] K. Devendranath et al., Effect of optimal weld parameters in the microstructure and mechanical properties of autogenous gas tungsten arc weldments of super-duplex stainless steel UNS S32750, Mater. Des., 66 (2015) 356-365.

[58] J.C. Jorge, L.F. Souza, and J.M. Rebello, The effect of chromium on the microstructure/toughness relationship of C-Mn weld metal deposits. Materials Characterization, 47 (2001) 195-205.

[59] U. Gürol, O. Çoban, I.C. Coşar, and M. Koçak, Effect of the notch location on the Charpy-V toughness results for robotic flux-cored arc welded multipass joints. Materials Testing, 64 (9) (2022) 1278-1289.

[60] S. Saravanan et al., Pulsed Nd: YAG laser welding and subsequent post-weld heat treatment on super duplex stainless steel, J. Manuf. Process., 25 (2017) 284-289.

[61] A. Pramanik, G. Littlefair, and A.K. Basak, Weldability of duplex stainless steel, Mater. Manuf. Process., 30 (9) (2015) 1053-1068.

[62] E. Capello et al., Laser welding and surface treatment of a 22Cr–5Ni–3Mo duplex stainless steel, Mater. Sci. Eng. A, 351 (1-2) (2003) 334-343.

[63] H.C. Wu, L.W. Tsay, and C. Chen, Laser beam welding of 2205 duplex stainless steel with metal powder additions, ISIJ Int., 44 (10) (2004) 1720-1726.

[64] R. Lai et al., Influence of absorbed nitrogen on microstructure and corrosion resistance of 2205 duplex stainless steel joint processed by fiber laser welding, J. Mater. Process. Technol., 231 (2016) 397-405.

[65] M. Ravichandran et al., Investigation on TIG welding parameters of 2205 duplex stainless steel, Int. J. of Automotive and Mech. Eng., 14 (2017) 4518-4530.

[66] A.B. Naik and A.C. Reddy, Experimental analysis of TIG welding and comparison between activated-TIG and TIG on duplex stainless steel (2205), Int. J. of Scientific & Eng. Res., 7 (6) (2016) 115-122.

[67] Z. Sun et al., Effect of dual torch technique on duplex stainless steel welds, Mater. Sci. Eng. A, 356 (2003) 274-282.

[68] G.L. Leone and H.W. Kerr, The ferrite to austenite transformation in stainless steels. Weld. J., 61 (1982) 13s-22s.

[69] J.W. Fourie and F.P.A. Robinson, Literature review on the influence of weld-heat inputs on the mechanical and corrosion properties of duplex stainless steels, J. S. Afr. Inst. Min. Metall., 90 (1990) 59-65.

[70] H. Sieurin and R. Sandstrom, Austenite reformation in the heat-affected zone of duplex stainless steel 2205, Mater. Sci. Eng. A, 418 (2006) 250-256.

[71] T. Küçükömeroğlu et al., Microstructure and mechanical properties of friction stir welded St52 steel joints, Int. J. Miner. Metall. Mater., 25 (12) (2018) 1457-1464.

[72] G. Çam et al., Investigation into properties of laser welded similar and dissimilar steel joints, Sci. Technol. Weld. Join., 3 (4) (1998) 177-189.

[73] G. Çam et al., Microstructural and mechanical characterization of friction stir butt joint welded 63%Cu-37%Zn brass plate, Weld. J., 88 (11) (2009) 225s-232s.

[74] J. Dos Santos et al., Properties of power beam welded steels, Al- and Ti-alloys: Significance of strength mismatch, Welding in the World, 44 (6) (2000) 42-64.

[75] G. İpekoğlu and G. Çam, Formation of weld defects in cold metal transfer arc welded 7075-T6 plates and its effect on joint performance, IOP Conf. Series: Mater. Sci. Eng., 629 (2019) 012007.

[76] G. İpekoğlu et al., Investigation of the effect of temper condition friction stir weldability of AA7075 Al-alloy plates, Mater. Tehnol., 46 (6) (2012) 627-632.

[77] G. Çam et al., Mechanical properties of friction stir butt-welded Al-5086 H32 plate, Mat.-wiss. u. Werkstofftech., 40 (8) (2009) 638-642.

[78] G. Çam, Prospects of producing aluminum parts by wire arc additive manufacturing (WAAM), Materials Today: Proceedings, 62 (1) (2022) 77-85.

[79] G. Çam, et al., Characterization of laser and electron beam welded Al-alloys, Prakt. Metallogr., 36 (2) (1999) 59-89.

[80] H. Yavuz and G. Çam, A novel welding technique: Friction stir welding, Endüstri ve Otomasyon, 51 (2001) 18-20.

[81] G. Çam et al., Fracture behaviour of diffusion bonded bimaterial Ti-Al joints, Sci. Technol. Weld. Join., 2 (3) (1997) 95-101.

[82] M. Koçak, M. Pakdil, and G. Çam, Fracture behaviour of diffusion bonded Ti-alloys with strength mismatch, Sci. Technol. Weld. Join., 7 (4) (2002) 187-196.

BMSM

Bulletin of Materials Science & Metallurgy

Periodical Scientific Journal of UCTEA Chamber of Metallurgical and Materials Engineers

Volume 1, Issue 2, 2024, Pages 11-15 Received: 25 March 2024 Accepted: 30 May 2024

Research Article

Monitoring and adjustments of combustion parameters in reheating furnaces using a digital tool

Kássio N. Cançado[a*], Ana Carolina Rocha[b], Rafaela Rapalo[c], Paula Pomaro[d], LismSoares[e]

[a] Federal University of Minas Gerais, Ph.D. student, Energy Efficiency Engineer, E&S, Vetta | SMS group, Brazil.

[b] Federal University of Minas Gerais, Master student, Energy Efficiency Trainee, E&S, Vetta | SMS group, Brazil.

[c] Federal University of Minas Gerais, Bachelor, Energy Efficiency Engineer, E&S, Vetta | SMS group, Brazil.

[d] Federal University of Minas Gerais, Master, Energy Efficiency Engineer, E&S, Vetta | SMS group, Brazil.

[e] Federal University of Minas Gerais, Ph.D., Head of Engineering, E&S, Vetta | SMS group, Brazil

*Corresponding author's email: kassio.cancado@vetta.digital

Abstract

Improving the energy efficiency of a reheating furnace is not a simple task because it involves a large number of parameters that, most of the time, are connected in a complex way. To be feasible, the evaluation of such a vast number of variables must be supported by digital tools that are embedded with artificial intelligence. The SMS group has developed a digital tool that effectively supports operators and engineers in enhancing energy efficiency within the reheating furnaces of hot rolling mills. This paper presents a quick study case of the use of *Viridis Performance*, an application of *Viridis Energy & Sustainability Suite*, in the analysis and correction of the deviations in the air-gas ratio of a reheating furnace. In this study, a production period of 8 hours was evaluated, during which the air-gas ratio presented a significant deviation. Analysis showed that the probable cause of the deviation was a production stoppage where the furnace control was set to manual mode. A reduction potential of 0.26 Gcal/h and a 13 kg/h decrease in CO_2 emissions were identified. *Viridis Performance* would support the process by guiding the decisions of the operator in a way that energy losses would be avoided or minimized. The potential economic savings were also quantified. This task is performed in the system by *Viridis Moneybox*, which is another application of *Viridis Energy & Sustainability Suite*. The results showed potential savings of 13 US $/h. In addition to the gains and savings outlined in this study, the utilization of *Viridis Performance* encompasses numerous other advantages, such as enhanced operational standardization and improved process capability, to name just a few.

Keywords

Digital tool, Reheating furnace, Combustion, Energy efficiency

1. Introduction

World energy consumption has been increasing continuously in recent decades, showing an increase of 11% in 2020 compared to 2019. Industrial energy consumption increased by 8% in the same period, representing 62% of world energy consumption [1]. Steel production is one of the most energy-intensive industrial processes, with a consumption equivalent to 18% of the world's energy [2]. Although the most significant consumers in the steel production chain are concentrated in upstream processes, such as blast furnaces, basic oxygen furnaces, and electric arc furnaces, energy consumption in downstream processes is far from insignificant. Among downstream processes, hot rolling is one of the largest sources of energy consumption [3].

In this context, due to their wide applicability, the reheating furnaces' energy consumption and efficiency is a topic of interest for several reasons, including:

- Important cost driver;
- An important emission source;
- Indirect influence on product quality.

The increase in energy efficiency of heating furnaces has been the subject of study in several papers in the literature:

Chen, Chung, and Liu [6] evaluated the energy consumption and performance of reheating furnaces in a hot strip mill through numerical predictions and practical measurements. The results showed that heat recovery systems correspond to 15% of the furnace's energy input, highlighting the importance of maintenance and correct management of this equipment. Khalid et al. [7] evaluated combustion with oxygen enrichment for reheating furnaces to reduce natural gas consumption in pusher furnaces. The results suggest that oxygen enrichment in the reheat furnace can significantly impact the environmental performance of the hot mill and contribute to the transition to steelmaking with a lower carbon footprint. Schmitz et al. [8] compared a state-of-the-art natural gas-fired reheating furnace to an electric heating furnace, a hydrogen-air heating furnace, and finally to a heating furnace, hydrogen-oxygen heating. The results showed significant potential for reducing CO_2 emissions, depending on the country's specific electricity production mix and future expansion of renewable energy sources. Furthermore, increasing H_2 production efficiency will reduce primary energy consumption and CO_2 emissions for reheating furnaces.

Digitalization is a keyword within the concept of Industry 4.0, along with the continuous search for increased energy efficiency and productivity. Digital tools, through real-time systems integration, provide increased productivity and cost reduction, greater process consistency, continuous quality monitoring, reduced breakdowns through monitoring of critical parameters, greater understanding of processes and equipment, and increased operational standardization through constant tracking of specific goals, among other things.

The present work will use a digital tool, *Viridis Performance*, to perform an exploratory analysis of the main reheating furnace process parameters, such as air-gas ratio during transient periods, to identify deviations, increase energy efficiency, and reduce energy consumption.

Viridis Performance is a digital tool from the SMS group embedded with state-of-the-art methodologies based on artificial intelligence and mathematical models. It ensures that energy efficiency actions are applied daily, reducing energy costs without equipment modification or production disruption.

2. Methodology

The methodology proposed in this work consists of performing an energy balance on a real operating scenario of a reheating furnace and a subsequent analysis of deviations that could be avoided using Viridis Performance. The reheating furnace is of the walking beam type and operates with coke furnace gas (COG). The methodology was divided into the following subsections: "Energy Balance" and "Analyses," as shown below.

2.1. Energy Balance

The energy balance used in this study follows the first law of thermodynamics [9]. The control volume is given in Figure 1, and the energy balance is defined by equations 1 to 7.

$$\dot{E}_{in} = Cs_{air} + Cs_{fuel} + \Delta Hc_{fuel} \quad (1)$$

$$\dot{E}_{out} = Cs_{fumes} \quad (2)$$

$$\Delta E = \dot{E}_{in} - \dot{E}_{out} \quad (3)$$

$$\Delta Hc_{fuel} = \sum_{i=1}^{k} fuel\,(i) + O_2 \xrightarrow{\Delta h0} CO_2 + H_2O \quad (4)$$

$$Cs_{air} = \sum_{i=1}^{k} Cs_{air}(i)_{@Tair\,[°C]} - Cs_{air}(i)_{@25\,[°C]} \quad (5)$$

$$Cs_{fuel} = \sum_{i=1}^{k} Cs_{fuel}(i)_{@T_{fuel}\,[°C]} - Cs_{fuel}(i)_{@25\,[°C]} \quad (6)$$

$$Cs_{fume} = \sum_{i=1}^{k} Cs_{fumes}(i)_{@Tfumes\,[°C]} - Cs_{fumes}(i)_{@25\,[°C]} \quad (7)$$

In which $\dot{E}_{in}$ is the input energy defined by Eq. (1), in (kcal/h); $\dot{E}_{out}$ is the output energy defined by defined by Eq.(2), in (kcal/h); ΔE is the available energy balance defined by Eq.(3), in (kcal/h); Cs_{air} is the sensible heat from air defined by Eq.(5), in (kcal/h), whose components are listed Table 2; Cs_{fume} is the sensible heat from the fumes defined by Eq.(7), in (kcal/h), whose components are listed in Table 3; Cs_{fuel} and ΔHc_{fuel} are the sensible heat and the fuel combustion energy defined by Eq. (6) and Eq. (4), respectively, and whose components are listed in Table 1.

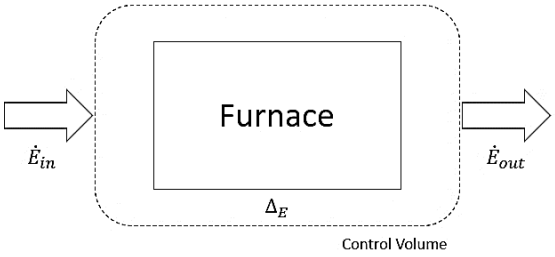

Figure 1. Energy balance control volume

Table 1. Fuel gas composition

		% Volumetric
1	CO_2	2.9
2	N_2	6.5
3	H_2	57.9
4	CO	7.5
5	CH_4	23.2
6	C_2H_6	2.2

Table 2. Air gas composition

		% Volumetric
1	O_2	21
2	N_2	79

Table 3. Fumes composition

CO_2
H_2
N_2
O_2
H_2O

2.2. Analyses

Subsequent analyses are made for a billet reheating furnace of the walking beam type that operates with coke furnace gas (COG). Such analyses are based on a typical production day.

As shown in Figure 2, the air-gas ratio remains at the same level most of the time. However, a significant deviation is evident between 4 am and 12 pm. The native resources of *Viridis Performance* were used to conduct an exploratory analysis for the period and determine the cause of this deviation.

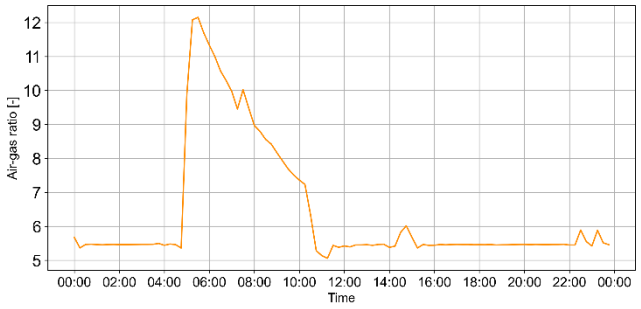

Figure 2. The air-gas ratio for one production day

The reheating furnace operates with COG, which is a by-product gas and, as such, may have its availability affected by process events. In case of unavailability and/or low availability of this gas, it is possible to use natural gas to supply the energy demand of the furnace, which changes the air-gas ratio. To evaluate if the air-gas ratio was changed due to a change in the fuel, the variation of the lower heating value (LHV) was plotted for the analyzed period, as shown in Figure 3. As can be seen, the maximum LHV variation was less than 5%, which does not indicate a fuel change.

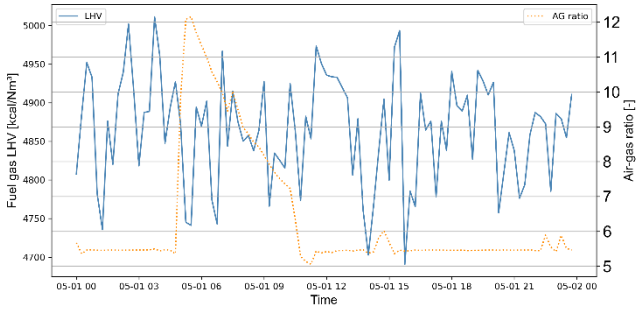

Figure 3. COG LHV variation

The next point to be checked is the production rate of the furnace. As seen in the graph of Figure 4, there is a stoppage in the furnace charge when the air-gas ratio presents a deviation. The curve in blue refers to an incremental scale that records the mass of the billets loaded into the furnace. Thus, the flat levels indicate periods when the billet charge was not recorded. The sudden drop in the graph shows the shift change period when the incremental counter is reset. The usage of *Viridis Performance* allowed a crosscheck of this hypothesis with production management data to confirm this assumption.

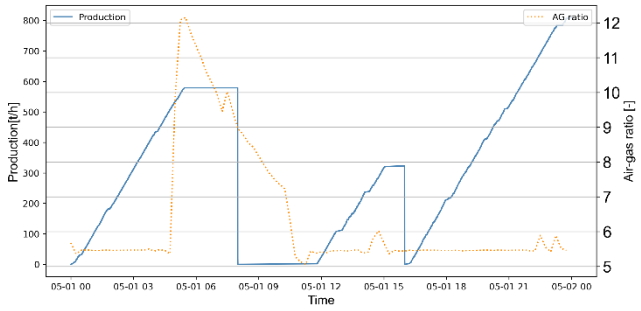

Figure 4. Reheating furnace production rate

Figure 5 shows that the operator manually reduced the furnace temperature during the stoppage. This hypothesis is validated by observing the temperatures of the control zones. The dashed line shows the setpoint of the control zones remained constant, while the value measured by the control thermocouples indicates a drop in the temperature (solid line). The additional analysis of air and fuel flows in each control zone shows a reduction for both, but the air-gas ratio was not maintained.

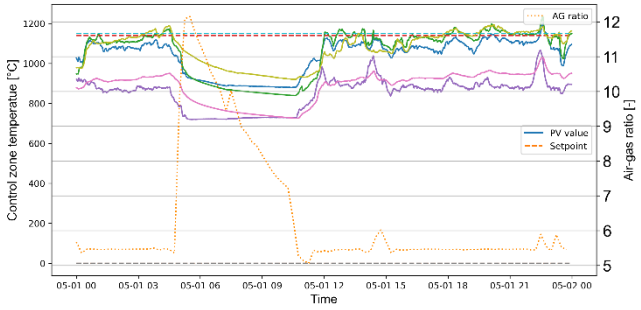

Figure 5. Control zones temperature

It is unclear whether the standard operational procedure requires a change to manual operation in case of prolonged stoppages. However, the reduction in the furnace temperature could have been achieved by keeping the air-gas ratio constant with lower energy input. Using *Viridis Performance's* resources to carry out the energy balance, whose methodology was previously described, it is possible to quantify the impact of this approach. The results found in the energy balance will be discussed in the next section.

3. Results and Discussion

An energy balance was performed for two different scenarios. The first refers to the actual production period discussed in the previous section. The second aims to quantify what energy input ($\dot{E}_{in}$, Eq. (3)) is needed to maintain the same net energy (ΔE, Eq. (3)) of scenario one if the air-gas ratio were kept at the same level before the deviation.

Table 4 shows the operational parameters used in the energy balance. The actual average values shown in the previous section were used for scenario one. For scenario 2, historical data were used, whose operation took place in conditions similar to those analyzed. For this purpose, *Viridis Performance* was used to define representative values from similar scenarios. The values of free oxygen in the fumes were calculated through the stoichiometric analysis of combustion.

Table 4. Energy balance parameters

Scenario	Avg. AG ratio	Fumes O_2 level	Air temp.	Fumes temp.
1	8:1	11%	260 °C	500 °C
2	5:1	4.7%	350 °C	650 °C

Table 5 summarizes the energy balance results for the two scenarios.

Table 5. Energy balance results

Scenario	$\dot{E}_{in}$ [Gcal/h]	ΔE [Gcal/h]	$\dot{E}_{out}$ [Gcal/h]	CO2 [Kg/h]
1	6.95	4.79	2.16	1085
2	6.69	4.79	1.9	1072

Analyzing the results, it can be concluded that by reducing the air-gas ratio from 8:1 to 5:1, the energy input necessary to maintain the same net energy in the furnace (ΔE = 4.79 Gcal/h) is decreased by 3.74% (0.26 Gcal/h). This occurs because, although the temperature of the fumes is higher in scenario two compared to scenario 1, the flue gas flow rate is significantly lower, which results in a decrease of 12% in energy loss through the fumes. The higher fumes temperature also results in a higher combustion air temperature, contributing to lower fuel demand.

Reducing energy consumption is a direct benefit of better control of combustion parameters. In addition to reducing gas consumption, lower CO_2 emissions are a secondary benefit. Performing the stoichiometric combustion analysis, scenario 2 emits 1.2% (13 kg/h) less CO_2 than scenario 1. Figure 6 and Figure 7 show the energy balance results.

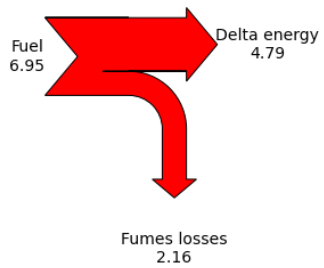

Figure 6. Energy balance results for scenario one

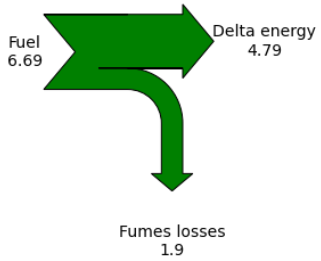

Figure 7. Energy balance results for scenario two.

4. Conclusion

The present work used *Viridis Performance* to identify deviations in the combustion parameters of a billet reheating furnace. *Viridis Performance* is an application of the *Viridis Energy & Sustainability Suite* that allows the real-time monitoring of hundreds of parameters through artificial intelligence resources and machine learning techniques. It enables the calculation and control of several indicators applied to different contexts, such as production levels, product mixes, etc.

A period of 8 hours was identified in which the air-gas ratio of the reheating furnace showed a significant deviation. Using native resources of *Viridis Performance*, an exploratory analysis was performed indicating that the probable cause of this deviation was a production stoppage where the operator placed the furnace control system in manual mode, and the adopted procedure to reduce the energy input did not keep constant the air-gas ratio. Through an energy balance, a potential energy saving of up to 3.7% was identified only by controlling the AG ratio. In addition, a reduction of 1.2 in the amount of CO_2 emitted would be possible.

Viridis Performance can continuously monitor hundreds of parameters, triggering alerts and checklists for the operator in case of deviations. In the case presented here, for example, when detecting a deviation in the air-gas ratio, the system would have triggered an alert and a checklist of corrective measures, guiding the operator to follow the operating standard. In cases where the deviation persists, new alerts are triggered, which can, for example, be configured so that alerts can be forwarded to the operation supervisor and/or to the operation management.

Another feature of the *Viridis Energy & Sustainability Suite* is the *Viridis Moneybox*. *Viridis Moneybox* prices the cost of each deviation from the operating standard. For example, taking a cost of 51 US $/Gcal as a reference, the potential reduction would be 13 US $/h only by controlling the AG ratio. Continuously pricing deviations are especially useful in defining the company's strategic plan and can be used as a benchmark for prioritizing projects and maintenance activities.

Declaration of Competing Interest

The authors declare that they have no known competing financial interests or personal relationships that could have appeared to influence the work reported in this paper.

References

[1] S. China National Bureau of Statistics, “Annual Data-Energy-Consumption of Total Energy by Sector.” Accessed: Feb. 11, 2023. [Online]. Available: data.stats.gov.cn/english/easyquery.htm?cn=C01

[2] P. Jin, Z. Jiang, C. Bao, S. Hao, and X. Zhang, “The energy consumption and carbon emission of the integrated steel mill with an oxygen blast furnace,” Resour. Conserv. Recycl., vol. 117, Aug. 2015, doi: 10.1016/j.resconrec.2015.07.008.

[3] G. D. Mistry and K. B. Judal, “Literature review of the stress, strain and separating force evaluation during hot bar rolling of different types of steels,” Mater. Today Proc., vol. 57, pp. 636–642, 2022, doi: https://doi.org/10.1016/j.matpr.2022.02.058.

[4] A. Steinboeck, D. Wild, and A. Kugi, “Feedback Tracking Control of Continuous Reheating Furnaces,” IFAC Proc. Vol., vol. 44, pp. 11744–11749, 2011.

[5] T. Morgado, P. J. Coelho, and P. Talukdar, “Assessment of uniform temperature assumption in zoning on the numerical simulation of a walking beam reheating furnace,” Appl. Therm. Eng., vol. 76, pp. 496–508, 2015, doi: https://doi.org/10.1016/j.applthermaleng.2014.11.054.

[6] W.-H. Chen, Y.-C. Chung, and J. Liu, “Analysis on energy consumption and performance of reheating furnaces in a hot strip mill,” Int. Commun. Heat Mass Transf., vol. 32, pp. 695–706, 2005, doi: 10.1016/j.icheatmasstransfer.2004.10.019.

[7] Y. Khalid et al., “Oxygen enrichment combustion to reduce fossil energy consumption and emissions in hot rolling steel production,” J. Clean. Prod., vol. 320, p. 128714, 2021, doi: https://doi.org/10.1016/j.jclepro.2021.128714.

[8] N. Schmitz, L. Sankowski, F. Kaiser, C. Schwotzer, T. Echterhof, and H. Pfeifer, “Towards CO2-neutral process heat generation for continuous reheating furnaces in steel hot rolling mills – A case study,” Energy, vol. 224, p. 120155, Jun. 2021, doi: 10.1016/J.ENERGY.2021.120155.

[9] Y. A. Çengel, Thermodynamics : an engineering approach. Sixth edition. Boston : McGraw-Hill Higher Education, [2008] ©2008. [Online]. Available: https://search.library.wisc.edu/catalog/9910062108002121

BMSM

Bulletin of Materials Science & Metallurgy

Periodical Scientific Journal of UCTEA Chamber of Metallurgical and Materials Engineers

Volume 1, Issue 2, 2024, Pages 16-25 Received: 18 March 2024 Accepted: 31 May 2024

Review Article

Review on Recent Progress in Wastewater Treatments via Using Alginate-Based Gels as Adsorbent Materials

Emircan Uysal [a], Emre Can Uysal [b], Halide Nur Dursun [a,c], Sebahattin Gürmen [a*]

[a] Department of Metallurgical and Materials Engineering, Istanbul Technical University, Istanbul, Türkiye

[b] Department of Chemistry Istanbul Technical University, Istanbul, Türkiye

[c] Department of Mineral Processing Engineering, Istanbul Technical University, Istanbul, Türkiye

*Corresponding author's email: gurmen@itu.edu.tr

Abstract

Wastewater constitutes a significant threat to human and environmental well-being owing to its high concentration of toxic compounds. The existence of heavy metal ions and organic pollutants in wastewater to an acceptable standard level is crucial. Adsorption, an economical, easily implementable, and eco-friendly method, is widely employed to eliminate targeted contaminants from wastewater. A wide array of adsorbent materials has been utilized throughout history, and novel functional materials continue to be developed. Biopolymers, characterized by their chemical structure, cost-effectiveness, environmental compatibility, biocompatibility, and biodegradability, have found applications in adsorption studies. Among these, alginate stands out due to its ability to form gels in the presence of divalent cations, facilitating the entrapment and removal of contaminants. Alginate, a biocompatible and biodegradable polysaccharide, is particularly utilized in adsorption processes due to its chemical properties. Alginate-based materials can form hydrogels, which provide a large surface area for adsorption and enhance the removal efficiency of heavy metals and organic pollutants. In addition to these advantages, alginate hydrogels may have low mechanical strength and, in some cases, may show undesirable dissolution tendencies. A variety of methodologies can be employed to eliminate weaknesses. This review delves into the use of alginate matrix gels for the removal of pollutants in wastewater, featuring an array of relevant studies. Moreover, a concise overview of the adsorption process, kinetics, and isotherms is provided.

Keywords

Adsorption, alginate gels, wastewater treatment

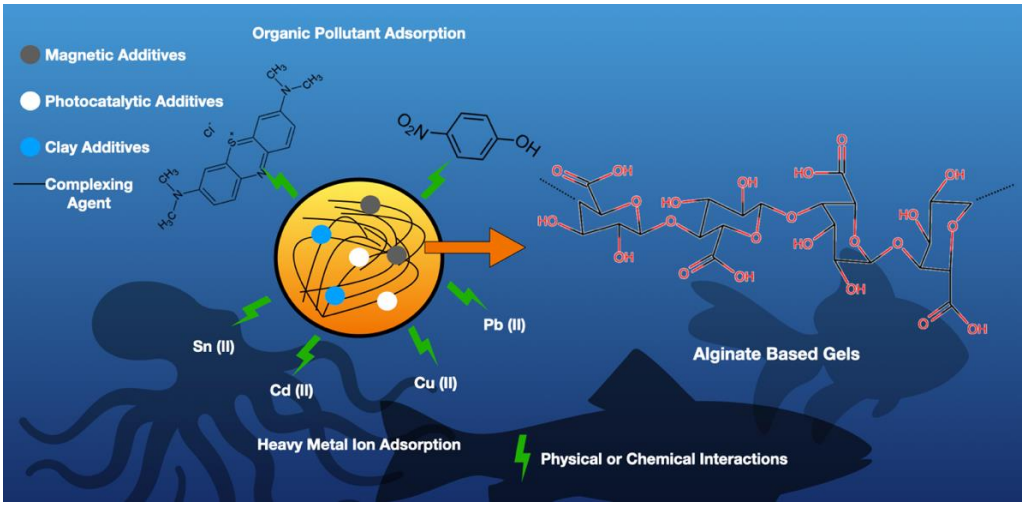

1. Introduction

With the advancement of technology, the growth of industrialization, and the rapid pace of urbanization, there has been a steady rise in the volume of wastewater generated daily. The pollutants present in wastewater pose substantial threats to both human health and the environment. Not only can these pollutants have toxic effects on the human body and lead to the development of cancer, but they also inflict severe damage on the natural surroundings. Consequently, it is imperative to effectively treat and purify the pollutants found in wastewater under specific standards. In addition to international organizations such as the World Health Organization (WHO), Food and Agriculture Organization (FAO), and European Union (EU), individual countries establish specific standards for water quality within their jurisdictions. FAO has provided guidelines on the acceptable levels of heavy metal ions in irrigation water, as outlined in Table 1. The presence of heavy metal ions in wastewater poses potential risks to both the ecosystem and human health. These heavy metals exhibit toxicity, and carcinogenic properties, and are non-biodegradable, thereby having the potential to contaminate water sources and jeopardize the well-being of individuals. Wastewater originating from various sectors including plating and electroplating, battery manufacturing, pesticide production, mining activities, tanning processes, textile manufacturing, metal smelting, petrochemical industries, paper production, and electrolysis applications is frequently found to contain significant concentrations of heavy metals [1]. Arsenic (As), cadmium (Cd), cobalt (Co), chromium (Cr), iron (Fe), manganese (Mn), nickel (Ni), lead (Pb), and zinc (Zn) are among the heavy metals commonly detected in wastewater [2]. Besides the heavy metal ions, organic contaminants present in wastewater have the potential to pose significant hazards to both the environment and public health. This category of pollutants encompasses a wide range of chemicals, such as dyes, humic substances, phenolic compounds, petroleum derivatives, surfactants, pesticides, and pharmaceuticals [3].

Before discharging wastewater into the natural environment, it is crucial to ensure that the levels of pollutants, including metal ions and organic contaminants, are reduced to below-specified thresholds. Various wastewater treatment methods can be employed to achieve this objective. These methods encompass chemical precipitation, ion exchange, membrane filtration, electrochemical treatment technologies, and adsorption. Among these methods, adsorption stands out due to its notable advantages. Some of these advantages include low cost, ease of implementation, and minimal environmental impact.

Table 1. FAO guidelines for heavy metals in irrigation water [4].

Heavy Metal Ion	*Recommended maximum concentration (mg/L)*	*Heavy Metal Ion*	*Recommended maximum concentration (mg/L)*
Al	5.00	Mn	0.20
As	0.10	Mo	0.01
Be	0.10	Ni	0.20
Cd	0.10	Pb	5.00
Co	0.05	Se	0.02
Cr	0.10	Sn	0
Cu	0.20	Ti	0
F	1.00	W	0
Fe	5.00	V	0.10
Li	2.50	Zn	2.00

The adsorption process refers to the phenomenon where the desired substance from a solution is selectively deposited onto the surface of a material known as the adsorbent. Throughout history, a wide range of adsorbent materials has been employed for wastewater treatment. Among these materials, ceramic-based substances have been utilized since ancient times owing to their remarkable adsorption capacity. Presently, researchers are actively involved in the development of materials that exhibit characteristics such as low cost, ease of processing, and high adsorption capacity. The aim is to create advanced adsorbent materials that are efficient and economical for wastewater treatment purposes. Biopolymers are used in many different applications such as adsorption processes due to their chemical properties, easy processability, low cost, biocompatibility, and biodegradability. Alginate is a low-cost, easily processable, biocompatible, and biodegradable polysaccharide obtained from brown algae cells. In addition to these advantages, it contains too many -OH groups in its chemical structure, which increases the adsorption efficiency with secondary interactions with alginates. Furthermore, its chemical structure can be readily modified following the desired properties. Moreover, these advantages, alginates have low thermal resistance, low pH stability, and mechanical strength. These drawbacks can be mitigated by incorporating additional complexing polymers (such as Chitosan, Gelatin, PVA), inorganic particles, and nanofiber reinforcement into the alginate matrix. Alginates can be gelled by chemical and physical methods; if it contains water in its structure, this gel is called hydrogel, if it is dried in an open atmosphere with heat, it is called xerogel, if it is dried by processes such as freeze drying, it is called cryogel, and if it is dried with supercritical fluids, it is called aerogel. Alginate

gels are frequently used in adsorption processes. Different materials are added to increase the adsorption capacity and improve the mechanical, thermal, and low pH stabilization properties.

This -review aims to provide a comprehensive overview of recently developed alginate-based adsorbent gel studies. this review, we delve into various strategies employed to enhance the adsorption capacity of alginate-based gels, shedding light on the physical and chemical modifications implemented. Additionally, this review provides a concise overview of the chemical structure of alginate, highlighting its linear copolymer nature consisting of (1→4)-linked β-D-mannuronic acid (M) and α-L-guluronic acid (G) residues. The relative composition of these residues in the alginate chain influences its physicochemical properties. Furthermore, the review touches upon the adsorption kinetics and isotherms of alginate-based gels. An understanding of adsorption kinetics aids in optimizing the adsorption process by determining the rate at which adsorption occurs. Isotherm models, such as the Langmuir and Freundlich models, are utilized to describe the equilibrium adsorption behaviour of alginate gels and provide valuable insights into the adsorption capacity and affinity. This review offers a comprehensive examination of recently developed alginate-based adsorbent gels. Exploring various strategies to enhance adsorption capacity and elucidating the physical and chemical properties, provides valuable insights for researchers and practitioners working in the field of adsorption science and technology.

2. Adsorption Kinetic Models and Isotherms

The material that adsorbs the target structure on its surface during the adsorption process is called adsorbent material. The adsorption process refers to the accumulation of the target structure on the surface of the adsorbent material. The efficiency in an adsorption process can be calculated by Equation 1;

$$Adsorption\ Efficiency\ (\%) = \left(\frac{C_0 - C_e}{C_0}\right) * 100 \qquad (1)$$

Here, C_0 is the initial pollutant concentration (mg. L^{-1}), and Ce is the pollutant concentration in the solution (mg. L^{-1}) in the equilibrium state of the system. The adsorption capacity of the adsorbent can be calculated using Equation 2;

$$q_t = (C_0 - C_t) * \frac{V}{M} \qquad (2)$$

In the equation, q_t is the adsorption capacity at a certain time (mg. g^{-1}), C_0 is the initial concentration (mg. L^{-1}), C_t is the concentration of the solution at a certain time (mg. L^{-1}), V is the solution volume (L), and M is the amount of adsorbent (g) indicates. Furthermore, many mechanisms are effective in this process; these can be physical interactions or chemical interactions. Concentration gradient, diffusion, and chemical interactions can be limiting factors of the adsorption process. Different kinetic modes have been developed to find the limiting factor in an adsorption process. Among the kinetic models, the most widely used are pseudo-first-order and pseudo-second-order. Linearized pseudo-first-order is expressed by Equation 3 [5];

$$ln(q_e - q_t) = Lnq_e - K_1 t \qquad (3)$$

In this equation, q_e and q_t represent the adsorption capacity (mg. L^{-1}) at equilibrium and "t" moment, respectively, K_1 is the equation constant and t is the time (minute). The pseudo-first-order equation gives the rate of change of ion adsorption with time. K_1 and qe values were calculated by plotting $Ln(q_e-q_t)$-t. The linearized version of the pseudo-second-order is expressed by Equation 4 [5];

$$\frac{t}{q_t} = \frac{1}{K_2 q_e^2} + \frac{t}{q_e} \qquad (4)$$

The variables here are the same as the pseudo-first-order equation. In adsorption studies that fit the pseudo-second-order, it is accepted that the rate limiter is chemisorption. K_2 and q_e values are calculated by plotting the change of t/q_t value concerning t. In addition to kinetic models, different Isotherms have been developed to explain the interaction between adsorbent and adsorbance. The two most commonly used isotherms; Langmuir and Freundlich. Langmuir isotherm can be expressed by Equation 5 [6];

$$\frac{1}{q_e} = \frac{1}{K_L q_m C_e} + \frac{1}{q_m} \qquad (5)$$

Here C_e is the equilibrium concentration (mg. L^{-1}), qm is the maximum adsorption capacity of the adsorbent (mg. g^{-1}), and K_L is the Langmuir constant. For adsorption studies conforming to the Langmuir model, it can be said that homogeneous adsorption takes place in the monolayer and on the surface of the adsorbent. With Equation 6, the relationship between Freudlich isotherm and experimental data can be examined [6];

$$\log(q_e) = \frac{1}{n_f}\log(C_e) + \log(K_f) \qquad (6)$$

Here, unlike the Langmuir isotherm, K_f is the Freudlich constant and n_f is the Freudlich isotherm constant, which gives an idea about the adsorption availability. Processes conforming to the Freundlich isotherm take place in a multilayer and heterogeneous manner. All these processes are explained by examining the fit between experimental data and models. Derived from the integral equation approach, which offers a simple and useful method for investigating adsorption on heterogeneous surfaces composed of energetically different patches distributed throughout the surface, the Langmuir–

Freundlich equation (Equation 7) mathematically expresses this approach [7].

$$\theta_e = \int_0^{\infty} \theta(E, P_e, T) \times (E) dE \quad (7)$$

Here, θ(E, Pe, T) represents a classical isotherm for adsorption on each patch with identical sites and the same adsorption energy E, while χ(E) is a normalized differential energy distribution function. Figure 1 gives a schematic representation of the energy distribution of adsorption on homogeneous and heterogeneous surfaces of a porous adsorbent material.

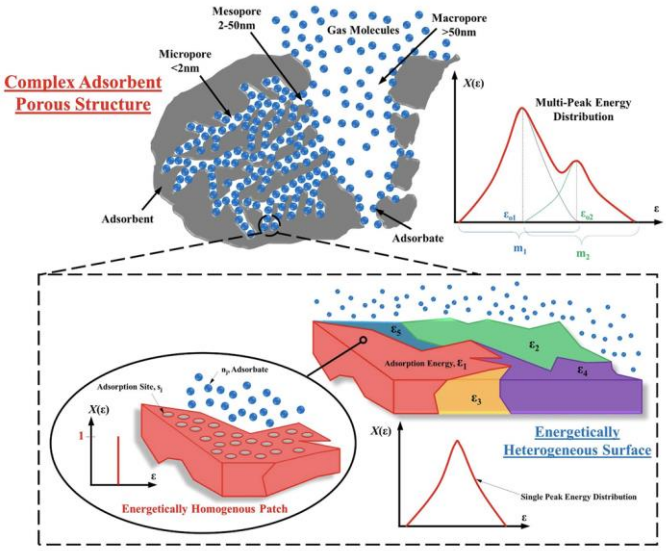

Figure 1. Schematic representation of the energy distribution of heterogeneous and homogeneous surfaces occurring on the surface of the porous adsorbent material [8].

In addition to all these, parameters such as temperature, time, solid-liquid ratio, and pH are effective in the adsorption process, and the effect of these parameters on the process should be examined. The effect of temperature on adsorption significantly affects both the adsorption rate and capacity. The adsorption rate increases strongly as the temperature increases due to the increasing kinetic energy of the adsorbate molecules [9]. However, adsorption capacity maybe decreases as temperature increases; this indicates that there is an exothermic process and the adsorptive forces between the active sites on the adsorbent surface and the pollutant material are weakened [9]. If the adsorption process is an endothermic reaction, the adsorption capacity will tend to increase [10]. Thermodynamic parameters (enthalpy, entropy, and Gibbs free energy) can be estimated from adsorption data, providing insights into adsorption mechanisms and can be used for process modification and optimization. In addition, the pH of the solution significantly affects the adsorption process, affecting both the surface charge of the adsorbent and the adsorption mechanisms [11]. The surface charge can be positive or negative depending on pH, and this charge is critical to the adsorption process. The point of zero charge (PZC), where the surface of the adsorbent is neutral, is important as it determines the surface chemistry and reactivity [11]. By changing ion adsorption, pH affects the availability and speciation of ions and also affects the hydrolysis and complexation reactions between metal ions and the adsorbent, thus changing the adsorption efficiency. Additionally, pH changes the adsorption rate and capacity by affecting the kinetic energy of adsorbate molecules and the availability of adsorption sites on the adsorbent surface. This is particularly important for applications such as heavy metal removal and biosorption, because optimizing pH can significantly increase adsorption efficiency and effectiveness.

3. Alginate as a Biopolymer

Natural polymer-based adsorbents offer a promising alternative to conventional adsorbents in renewability, recyclability, and tunable physicochemical properties [12]. Alginate, lignin, cellulose, and chitosan are generally low-cost biopolymers. Due to its high biodegradability, biocompatibility, and environmentally friendly nature, alginate is widely used as adsorbent material for different inorganic and organic pollutants. However, the low-temperature thermal degradation of sodium alginate [13] and poor stability [14] limit its use in different applications. Therefore, it is necessary to develop alginate to remove pollutants from wastewater.

Alginate refers to a family of linear polysaccharides, such as alginic acid and alginate salts, composed of β (1→4) linked β-d-mannuronic acid (M) residues and the C-5 epimer α l-guluronic acid (G). These monomers are arranged in an irregular block, consisting of homo-sequences of consecutive M or G residues (M- or G-blocks) alternating with G/M hetero-sequences (see Figure 2). While M blocks add flexibility to the alginate structure, G blocks increase the rigidity of the alginate. Besides Mw, G/M ratio also affects the properties of alginate-based gels. The G/M ratio and Mw must be considered when examining the properties of alginate-based gels to be produced.

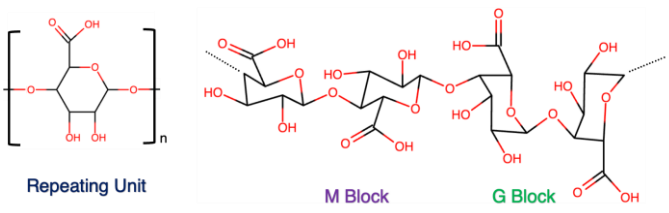

Figure 2. Chemical structure of alginate.

Alginate can be produced from brown algae cells in various forms. Sodium alginate is the form of alginate obtained from brown algae cells and is the sodium salt of alginic acid. It is

possible to extract alginate from brown algae cells as alginic acid, sodium alginate and calcium alginate. The extraction of alginate from seaweed is a multi-stage process that begins with washing, drying, and milling the seaweed, followed by rehydration and chemical treatments to remove unwanted compounds, then applying acid or alkali pre-treatment to break the plant cell wall and using sodium carbonate extraction to obtain water-soluble alginate, and finally recovering the alginate from the solution through sodium alginate, calcium alginate, or alginic acid precipitation methods [15]. Alginate extraction routes are presented in Figure 3.

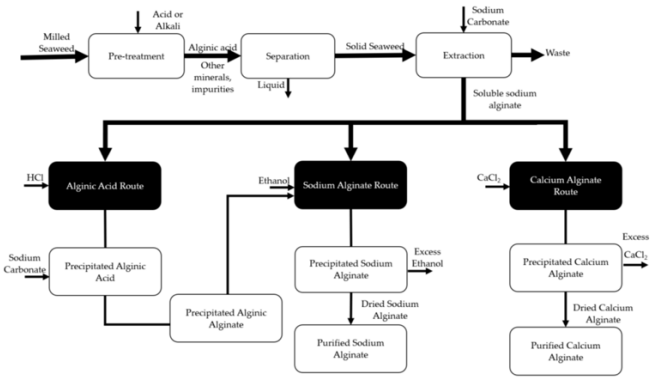

Figure 3. Alginate extraction routes from brown seaweed [15].

Alginates can form gels. Gelation can occur by ionotropic gelation or acid precipitation. Ionotropic gelation occurs when the negatively charged carboxyl parts of the alginate chains interact with multivalent cations or cationic polymers. The aqueous alginate solution, also called the "sol" phase, can be crosslinked by both divalent and trivalent cations [16]. Cross-linking of alginate leads to a "left to gel" transition resulting in the formation of alginate hydrogels that retain high water molecule content via hydrogen bonds [17]. The gelation kinetics and properties of the obtained hydrogels are mainly dependent on the properties of the ion such as valence electron and radius [18].

The interaction between polyvalent cations and alginate is described by the "eggbox" model. It is thought that electronegative vacancies, which can accommodate the cations of two G blocks consisting of adjacent chains, form "eggbox junctions" [19]. Before the crosslinking step, the "eggbox junctions" are occupied by alginate counterions such as sodium [20]. As a result of ion exchange, an "egg box" structure is formed. Although it is thought that only G blocks are involved in intermolecular crosslinking, MGM blocks may also contribute to gelation as a result of weak interactions with cations [21]. The egg box structure is given in Figure 4.

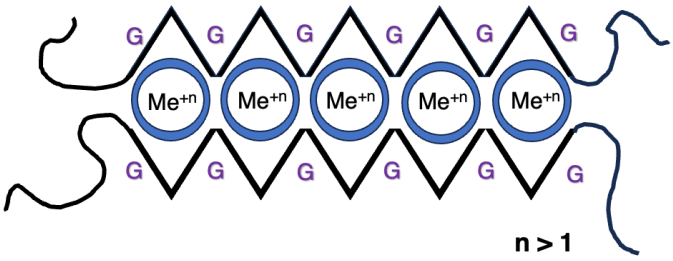

Figure 4. Egg-Box structure.

While the alginate solution is in its sol phase, different materials can be added to increase its performance. After doping the gels, it is passed from the sol to the gel. In this way, high-performance alginate-based hydrogels can be produced. These additives can be organic polymers, synthetic polymers, inorganic particles, or a combination of them. For example, while complex gels are formed by adding chitosan to increase the pH resistance of alginate, gelatin, and PVA to improve their mechanical properties, their properties can be improved by adding metallic or ceramic-based nanoparticles with different properties. In this mini-review, wastewater treatment studies by doping magnetic, photocatalytic, and clay-based materials into alginate or alginate complex gels are included. In the subsequent sections of the mini-review, a comprehensive analysis is provided regarding the elimination of organic and inorganic contaminants from wastewater using alginate-based gels that have undergone the gelation process.

4. Magnetic Particle Doped Alginate Gels

Adsorbent materials must be separated from the solution after removing the target compounds in the wastewater. Although the separation of macro-size (around cm-mm size) beads can still be easily separated by filtration methods, it is relatively difficult to separate micro and nano-size beads from the wastewater solution with filtration methods. The external magnetic field is acceptable as a promising easy and inexpensive method for separating adsorbent materials from wastewater solution. The addition of magnetic materials (Fe, Fe_3O_4, etc.) in gels with an alginate-based matrix ensures that these gels can be easily separated via the external magnetic field from the solution after the adsorption process. In their study, Ma et al. investigated the removal of dyes from wastewater through the incorporation of graphene oxide (GO) and iron oxide nanoparticles (Fe_3O_4) into alginate/chitosan gels [22]. Their findings revealed that the various functional groups present in the structure of GO are adsorbed onto the gels through secondary interactions with the dyes present in the wastewater. The inclusion of Fe_3O_4 was found to facilitate the subsequent solid/liquid separation process after adsorption. The researchers observed that the addition of GO and chitosan led to an increase in the surface area and porosity of the gels. However, the increased amount of chitosan had a negative

impact on the adsorption process. They attributed this phenomenon to the enhanced interaction between alginate and chitosan, which resulted in reduced penetration of the dye into the gel. Furthermore, the authors demonstrated that the adsorption process followed the pseudo-first-order kinetics, indicating that physical adsorption predominated. They also noted that the gels maintained their high adsorption capacity even after five cycles, suggesting their durability and potential for repeated use. Also, with the addition of magnetic material in this study, extra materials are used to increase the adsorption capacity of the gels. Zeng et al. reported that they developed adsorbent material by adding Fe_3O_4/maghemite nanoparticles into alginate/chitosan matrix aerogels [23]. They added iron mud as the main adsorption agent into the gel matrix. They studied the removal of phosphate ions in wastewater and observed time-varying adsorption kinetics. In this study, it was tried to eliminate the weak properties of alginate by using chitosan in addition to alginate. In addition to chitosan, different polymeric structures are also used to improve the properties of alginate. Zang et al. produced alginate/PVA hydrogels with the interpenetrating method in their work [24]. They claimed that the addition of PVA would increase the stability of the gels. They prepared PVA and sodium alginate solution and emulsified with Tween 80, Span 80, and Cyclohexane to form a microsphere. They added Fe^{2+} and Fe^{3+} ions to the solution they obtained, and then, by the addition of NH_4OH, the Fe_3O_4 particles were precipitated. They claimed that when $Fe^{2+/3+}$ ions were added and interacted with the carboxyl groups in the alginate, so they obtained smaller particles during precipitation. They studied the adsorption of different aromatic compounds from wastewater, such as salicylic acid, phenol, aniline, p-methoxy phenol, and p-nitrophenol, with the Fe_3O_4 added SA/PVA gel they obtained. They calculated the lowest adsorbent capacity at pH 7 with salicylic acid (almost 0 mg/g) and the highest adsorbent capacity when working with p-nitrophenol (78 mg/g). They claimed that this was due to the interaction of different aromatic compounds with the hydrophilic and hydrophobic parts of the gels. However, they explained that the adsorbent capacity varies at different pHs, and since the gels always have a negative zeta potential value in the pH 1-13 band, the alginate carboxylate groups change with pH, which is due to the change in hydrophilicity and hydrophobicity.

Furthermore, the weak mechanical properties of alginate can also be increased with different nanofiber reinforcements. Nanofibers increase the mechanical strength of nano-fiber composite gels by carrying the mechanical strength of the matrix. Salahuddin et al. reported that they carried out a wastewater (red mud solution) cleaning process by adding decorated cellulose nanofiber and Fe_3O_4 nanoparticles into the alginate hydrogel matrix [25]. They reported that the addition of cellulose nanofibers increased the mechanical strength of the gels. In addition, they noticed that the addition of Fe_3O_4 nanoparticles, produced by the co-precipitation method, with CNF to the alginate matrix increased the surface area and porosity of the gels. They reported that the addition of Fe_3O_4 nanoparticles had a positive effect on the wastewater treatment process, and that solid/liquid separation could be made easily by applying an external magnetic field after the process.

In a different approach, the properties of alginate gels can be improved by crosslinking with different agents instead of alginate Ca^{2+} ions. Wang et al. produced magnetic alginate-based aerogel with the addition of Fe_3O_4 in their gels, which is obtained by crosslinking sodium alginate with industrial alkaline residues [26]. They showed that crosslinking alginate with industrial alkaline residues provides a more homogeneous pore distribution during freeze drying, increases mechanical strength, and increases the adsorption efficiency. They attributed this to the fact that different metal ions in the alkaline residue show different gelation properties and that internal gelation occurs more slowly and homogeneously. They carried out Cd (II) removal from wastewater; they claimed that the adsorption kinetics were compatible with the pseudo-second-order, and the isotherm compatible with Langmuir. They repeated the process for 5 cycles and observed that around 90% of the material retained its effect.

The surfaces of the gels produced in the nanoscale can be modified by polymerization methods, which can lead to an increase in the adsorption capacity of the gels. Wu et al., in their study, coated Fe_3O_4@SiO_2 nanoparticles with alginate and gelled them with Ca^{2+} ions [27]. They modified the surfaces of the gels they produced with poly (ethylene imine) and polymerized benzyl dimethyl [2-[(2-methyl-1-oxoally) oxy] ethyl] (BDAC) ammonium chloride by free radical polymerization. They tried the adsorption of Diclofenac Sodium and Reactive Red X-3 compounds from wastewater with the presence of various functional groups of BDAC. They emphasized that the adsorption capacity of the gels increased significantly with the addition of BDAC. They showed that the isotherm of the adsorption process is compatible with Langmuir, and its kinetics with pseudo-second-order. They examined the interaction between adsorbent and adsorbed by FTIR and XPS analysis. They showed that the adsorption resulted from the electrostatic action, hydrogen bonding, and π-π interactions between the gel and the adsorbed.

Furthermore, the coating of nano-sized particles with different polymers is encountered in gels produced later in the form of polyelectrolyte with alginate in literature. Wang et al., in their study, coated Fe_3O_4 nanoparticles, which they produced with co-precipitation, with APTES [28]. With the presence of functional groups of the particles modified with APTES, they formed a polyelectrolyte with sodium alginate. The obtained complex structure was crosslinked with Ca^{2+} ions. Gradual

APTES and alginate coating of Fe_3O_4 particles increased the surface area and decreased the magnetic saturation value. They tried the removal of Pb^{2+} ions from wastewater and obtained an adsorbent capacity of 105.8 mg/g. They showed that the isotherm of the adsorption process was compatible with Langmuir, and the kinetic of the adsorption process was consistent with the pseudo-second-order. They performed adsorption with HCl acid and claimed that the material worked with 77% efficiency from 5 cycles.

Moreover, the magnetic particles provide easy separation of the gels from the solution, as well as increase the adsorption efficiency with the magnetic fields of the particles. The interaction of the ions in the solution (due to their charge) with the magnetic field has a positive effect on the adsorption capacity of the gels containing magnetic particles. Uysal et al. investigated the adsorption of Nd^{3+} ions from wastewater using Fe-based particles incorporated into alginate gels under the influence of a magnetic field [10]. To enhance the stability of the alginate-based gels under low pH conditions, chitosan was utilized as a coating agent. The adsorption process exhibited varying kinetic models at different time intervals. Initially, the adsorption followed a pseudo-first-order kinetic model, which later transitioned to a pseudo-second-order model. Toward the end of the adsorption process, the Elovich equation provided a suitable fit for the experimental data. The authors demonstrated that chemisorption played a dominant role in the adsorption process. The adsorption isotherm conformed to the Freundlich isotherm model, indicating heterogeneous adsorption involving multiple layers. Additionally, desorption studies were conducted, revealing that HCl acid exhibited the highest efficiency, while tartaric acid, an organic acid, showed promising results. The authors attributed this phenomenon to the complexation between tartaric acid and rare earth elements (REEs).

5. Photocatalytic Particle Doped Alginate Gels

Adding materials with photocatalytic properties into gels is an effective method for removing contaminants from the waste solution under solar and UV irradiation. Photocatalytic materials cause the scattering of rays of certain wavelengths with their band gaps. Photocatalytic degradation can be briefly expressed by the following Equation 8-18 [29];

$$Photocatalytic\ Gel + irradiation \rightarrow Photocatalytic\ Gel\ (h_{VB}^{+} + e_{CB}^{-}) \quad (8)$$

$$Pollutant\ Material + irradiation \rightarrow Pollutant\ Material^{*} \quad (9)$$

$$Pollutant\ Material^{*} + Photocatalytic\ Gel \rightarrow Pollutant\ Material^{\circ+} + Photocatalytic\ Gel\ (e_{CB}^{-}) \quad (10)$$

$$O_2 + Photocatalytic\ Gel\ (e_{CB}^{-}) \rightarrow Photocatalytic\ Gel + O_2^{\circ-} \quad (11)$$

$$O_2^{\circ-} + H^{+} \rightarrow HO_2^{\circ} \quad (12)$$

$$2HO_2^{\circ} \rightarrow O_2 + H_2O_2 \quad (13)$$

$$H_2O_2 + O_2^{\circ-} \rightarrow HO^{-} + HO^{\circ} + O_2 \quad (14)$$

$$H_2O_2 + e^{-} \rightarrow HO^{-} + HO^{\circ} \quad (15)$$

$$H_2O + Photocatalytic\ Gel\ (h_{VB}^{+}) \rightarrow Photocatalytic\ Gel + HO^{\circ} + H^{+} \quad (16)$$

$$HO^{-} + Photocatalytic\ Gel\ (h_{VB}^{+}) \rightarrow Photocatalytic\ Gel + HO^{\circ} \quad (17)$$

$$Pollutant\ Material + Photocatalytic\ Gel\ (h_{VB}^{+}, O_2^{\circ-}, HO^{\circ}) \rightarrow\rightarrow\rightarrow CO_2 + NO_2 + H_2O + other\ products \quad (18)$$

Irradiation of sunlight and UV onto photocatalytic gels leads to the formation of charge carriers and the transport of electron and hole pairs (e_{CB}^{-}/ h_{VB}^{+}). The pollutant structure, on the other hand, adsorbed on the surface of the photocatalytic gel absorbs energy and transfers the photogeneration electron to the conduction band of the gel. In interaction with these photogeneration electrons, surface-adsorbed oxygen (O_2) molecules are converted into superoxide radical anions ($O_2^{\bullet}$) and hydrogen peroxide radicals ($HOO^{\bullet}$). In addition, photogeneration holes (h_{VB}^{+}) combine with water molecules or hydroxyl anions on surfaces to form hydroxyl radicals ($HO^{\bullet}$) as a result of photocatalytic excitation. This photogeneration attacks the structure of the pollutant to convert active radical species into non-toxic molecules. The point to be considered in adsorption experiments is that performing the reaction under irradiation after adsorption in the dark without irradiation increases the yield.

TiO_2 nanoparticles are used in various applications as photocatalysts due to the band gap of structure. Chkirida et al., in their study, produced Ca alginate gels, added clay into the gels, coated the surface of the gels with TiO_2-P25 nanoparticles via non-thermal impregnation method, and reported that they removed Methylene Blue from wastewater under UV light [30]. Their gels' excellent photocatalytic function was proven by testing their ability to degrade COD (Chemical Oxygen Demand), a typical indication of organic contaminants in water. The COD is the quantity of oxygen required to oxidize the organic components in the water sample. They showed increased COD removal with UV light. Also, Dai et al. produced calcium alginate aerogels, furthermore they added TiO_2 nanoparticles to the alginate gel

matrix in their study [31]. With the addition of TiO_2, the pore size and surface area of the gels increased, and the UV resistance also increased. They tried to the separation of oil/water from wastewater with the gels they produced. They separated around 99% of soybean oil, hexane, kerosene, and pump oils from water. They also tried the adsorption of methylene orange (MO) via using UV irradiation, and they removed around 98% MO from wastewater. They claimed that even after 6 cycles of UV adsorption, the gels remained stable to a large extent. Moreover, doping TiO2 particles causes an increase in photocalistic properties. Chkirida et al. reported that by doping Fe_2O_3 and Fe_3O_4 to TiO_2 nanoparticles, they improved the photocatalytic properties of TiO_2 nanoparticles [32]. They produced calcium alginate microspheres containing TiO_2-Fe_2O_3 and TiO_2-Fe_3O_4 in 4 different ratios (1%, 2.5%, 5%, and 10%). They tried to remove MB from the wastewater with the gels produced, and they claimed that 80% of the wastewater was cleaned.

In addition to materials with suitable band gaps such as TiO_2, different materials are also used as photocatalysts. Materials with overlapping conduction and valence bands (without band gap), such as Ag nanoparticles, can radiate at certain wavelengths. This phenomenon is called surface plasmon resonance. Thanks to the electron configuration of noble metals, this radiation can be controlled by the number of electrons on the surface, which varies according to particle size and surface area. Ag nanoparticles are a material that exhibits photocatalytic properties with the phenomenon of surface plasmon resonance. For this reason, Ag nanoparticles are also used as an alternative to TiO_2 particles in wastewater cleaning processes. Hasan et al., in their study, produced complex gels with alginate and polyacrylonitrile and reported their findings on the removal of nitrophenols (DNP) compounds from wastewater by Ag nanoparticles in their gels [33]. They prepared a solution with sodium alginate precursor powder, then added $AgNO_3$ into the solution. After the reduction of metallic Ag nanoparticles in the solution was completed, acrylonitrile monomer and N, N-methylene bisacrylamide (crosslinker) were added to the solution, respectively. After completing the structural characterization of the complex gels, they produced, they used the response surface method to determine the most optimal parameters in the removal process of their compounds in wastewater. They claimed that a photocatalytic capacity of 99.46% could be obtained when the irradiation time was 35 minutes, the pH of the DNP solution was 4.68, and the DNP concentration was 70 mg L^{-1}.

6. Clay Particle Doped Alginate Gels

Clay-based materials are used in various applications due to their physical and chemical properties. Clay-based materials are frequently used in adsorption processes. Their chemical structures, crystal structures, and ionic charge balances make ceramic-based materials good adsorbent materials. They can adsorb on their surfaces by secondary interactions (such as Van der Walls, hydrogen bonds, etc.) with many materials such as water and organic-based structures. Also, their porous structure positively affects the adsorption capacity. Mundkur et al. reported doping clay materials into calcium alginate gels in different forms [34]. They produced clay-alginate beads, sodium carbonate-treated clay-alginate beads, clay-alginate-surfactant beads, and clay-alginate-nanoparticle (Fe_3O_4) beads and studied MB removal from wastewater. They achieved the removal of around 95% of MB in wastewater with the gels they produced, and they claimed that the adsorption kinetics fitted pseudo-second-order and isotherm compatible with Langmuir.

The montmorillonite crystal structure consists of 2 silica tetrahedral sheet sandwiches, the octahedral aluminum sheet of the middle part, and is also a ceramic material group with high water absorption capacity. Its chemical structure consists of Si, Al, Ca, Na, and Mg. Akın et al., in their studies, produced gelatin-alginate complex gel and doped montmorillonite and removed crystal violet from wastewater [35]. They prepared gelatin and sodium alginate solution, then added montmorillonite to this solution and homogenized it, then added it to the $CaCl_2$ solution. They optimized the optimum pH, temperature, and time for adsorption. They stated that the maximum adsorption capacity was reached for 120 minutes and it was suitable for adsorption at pH 7. They claimed that the adsorption isotherm is Langmuir, so the adsorption takes place homogeneously from mono-layer, and its kinetics is pseudo-second-order, that is adsorption by chemical interaction. They reported that the adsorption efficiency was 90.2% in the first cycle and that the yield decreased by 66.8% at the end of the 10^{th} cycle.

Bentonite is a ceramic material group consisting of Ca and Na montmorillonite, with high water absorption capacity and high adsorbent capacity. According to Yari et al., bentonite/Fe_3O_4 nanoparticles and sodium alginate may efficiently adsorb lead ions [36]. Four kinds of bentonite magnetic nanoparticles were produced in this work. Magnetic nanoparticles were then adsorbed on alginate to form beads for removing lead ions from synthetic pollution solutions. Adsorbent dose, pH values, stirring speeds, pollutant concentrations, and adsorption periods were all examined. The results show that 0.1 g of beads at a pH of 7, an adsorption duration of 8 hours, and a stirring velocity of 100 rpm provided the best conditions for removing Pb^{2+}. The beads showed a high adsorption efficiency of around 98%, and the adsorption process followed the Freundlich isotherm model. All alginate gels described in this review and their performance are summarized in Table 2.

Table 2. Different alginate-based gels and their adsorbent capacities.

Matrix	Additive	Pollutant Material	Adsorption Capacity (mg/g)	Reference
Sodium Alginate/ Chitosan	GO, Fe_3O_4	MB NR ST	21.325 44.654 44.313	16
Alginate/ Chitosan	Fe_3O_4, Fe_2O_3	Phosphate	18.5	17
Alginate/ PVA	Fe_3O_4	Aromatic Compounds	5-78	18
Alginate	CNF, Fe_3O_4	Al K Se Na V S	22 13.2 19 11.1 44.4 13.7	19
Alginate/Alkaline Residue	Fe_3O_4	Cd	38.83	20
Sodium alginate/ enzyldimethyl[2-[(2-methyl-1-oxoally) oxy] ethyl] ammonium chloride	Fe_3O_4@SiO_2	DS X-3B	340.58 370.85	21
Sodium Alginate/APTES	Fe_3O_4	Pb	105.8	22
Alginate/ Chitosan	Fe	Nd	6.72	23
Alginate	Clay-TiO_2	MB	-	25
Alginate	TiO_2	Oil	-	26
Alginate	Fe_3O_4 and Fe_2O_3 Doped TiO_2	MB	-	27
Alginate-g-Polyacrylonitrile	Ag	Nitrophenols	-	28
Alginate	Different Clays	MB	-	29
Sodium Alginate/ Gelatin	Montmorillonite	Crystal Violet	1000	30
Alginate	Bentonite, Fe_3O_4	Pb	-	31

7. Future Outlook

Due to its properties, alginate is a promising biopolymer in adsorption processes. With different doping, functional properties can be gained and adsorption efficiency can be increased. Alginate properties are improved with modifications made by chemical reactions and the addition of another complexing polymer, apart from doping. It is predicted that access to clean water will become increasingly difficult in the coming years. Wastewater, arising from the anthropogenic activities that have been established by humanity, necessitates treatment before its discharge into the natural environment. Alginate gels are promising in industrial-scale wastewater treatment processes due to their biodegradable and bioluminescent nature, low cost, and easy production.

Declaration of Competing Interest

The authors declare that they have no known competing financial interests or personal relationships that could have appeared to influence the work reported in this paper.

References

[1] N. A. A. Qasem, R. H. Mohammed, ve D. U. Lawal, "Author Correction: Removal of heavy metal ions from wastewater: a comprehensive and critical review", *npj Clean Water*, c. 4, sy 1, s. 52, Ara. 2021, doi: 10.1038/s41545-021-00144-z.

[2] B. F. Bakare ve G. C. Adeyinka, "Evaluating the Potential Health Risks of Selected Heavy Metals across Four Wastewater Treatment Water Works in Durban, South Africa", *Toxics*, c. 10, sy 6, s. 340, Haz. 2022, doi: 10.3390/toxics10060340.

[3] S. Mandal, A. Kunhikrishnan, N. S. Bolan, H. Wijesekara, ve R. Naidu, "Application of Biochar Produced From Biowaste Materials for Environmental Protection and Sustainable Agriculture Production", içinde *Environmental Materials and Waste*, Elsevier, 2016, ss. 73-89. doi: 10.1016/B978-0-12-803837-6.00004-4.

[4] "A compendium of standards for wastewater reuse in the Eastern Mediterranean Region", World Health Organization, 2006.

[5] H. Qiu, L. Lv, B. Pan, Q. Zhang, W. Zhang, ve Q. Zhang, "Critical review in adsorption kinetic models", *J. Zhejiang Univ. Sci. A*, c. 10, sy 5, ss. 716-724, May. 2009, doi: 10.1631/jzus.A0820524.

[6] M. A. Al-Ghouti ve D. A. Da'ana, "Guidelines for the use and interpretation of adsorption isotherm models: A review", *Journal of Hazardous Materials*, c. 393, s. 122383, Tem. 2020, doi: 10.1016/j.jhazmat.2020.122383.

[7] S. Azizian ve S. Eris, "Adsorption isotherms and kinetics", içinde *Interface Science and Technology*, c. 33, Elsevier, 2021, ss. 445-509. doi: 10.1016/B978-0-12-818805-7.00011-4.

[8] K. C. Ng, M. Burhan, M. W. Shahzad, ve A. B. Ismail, "A Universal Isotherm Model to Capture Adsorption Uptake and Energy Distribution of Porous Heterogeneous Surface", *Sci Rep*, c. 7, sy 1, s. 10634, Eyl. 2017, doi: 10.1038/s41598-017-11156-6.

[9] T. M. Budnyak *vd.*, "Chitosan Deposited onto Fumed Silica Surface as Sustainable Hybrid Biosorbent for Acid Orange 8 Dye Capture: Effect of Temperature in Adsorption Equilibrium and Kinetics", *J. Phys. Chem. C*, c. 124, sy 28, ss. 15312-15323, Tem. 2020, doi: 10.1021/acs.jpcc.0c04205.

[10] E. Uysal, E. Emil-Kaya, D. Yesiltepe-Ozcelik, ve S. Gurmen, "Nd Recovery from Wastewater with Magnetic Calcium Alginate ((1,4)-β-d-Mannuronic Acid and α-L-Guluronic Acid) Hydrogels", *ACS Omega*, c. 8, sy 19, ss. 16762-16778, May. 2023, doi: 10.1021/acsomega.2c08221.

[11] M. Kosmulski, "The pH dependent surface charging and points of zero charge. IX. Update", *Advances in Colloid and Interface Science*, c. 296, s. 102519, Eki. 2021, doi: 10.1016/j.cis.2021.102519.

[12] O. Duman, T. G. Polat, C. Ö. Diker, ve S. Tunç, "Agar/κ-carrageenan composite hydrogel adsorbent for the removal of Methylene Blue from water", *International Journal of Biological Macromolecules*, c. 160, ss. 823-835, Eki. 2020, doi: 10.1016/j.ijbiomac.2020.05.191.

[13] Y.-N. Phang, S.-Y. Chee, C.-O. Lee, ve Y.-L. Teh, "Thermal and microbial degradation of alginate-based superabsorbent polymer", *Polymer Degradation and Stability*, c. 96, sy 9, ss. 1653-1661, Eyl. 2011, doi: 10.1016/j.polymdegradstab.2011.06.010.

[14] Y. Liu *vd.*, "Photoreduction of Cr(VI) from acidic aqueous solution using TiO2-impregnated glutaraldehyde-crosslinked alginate beads and the effects of Fe(III) ions", *Chemical Engineering Journal*, c. 226, ss. 131-138, Haz. 2013, doi: 10.1016/j.cej.2013.04.048.

[15] S. Saji, A. Hebden, P. Goswami, ve C. Du, "A Brief Review on the Development of Alginate Extraction Process and Its Sustainability",

Sustainability, c. 14, sy 9, s. 5181, Nis. 2022, doi: 10.3390/su14095181.

[16] S. Boi *vd.*, "Alginate microbeads with internal microvoids for the sustained release of drugs", *International Journal of Biological Macromolecules*, c. 156, ss. 454-461, Ağu. 2020, doi: 10.1016/j.ijbiomac.2020.04.083.

[17] B. Reig-Vano, B. Tylkowski, X. Montané, ve M. Giamberini, "Alginate-based hydrogels for cancer therapy and research", *International Journal of Biological Macromolecules*, c. 170, ss. 424-436, Şub. 2021, doi: 10.1016/j.ijbiomac.2020.12.161.

[18] S. H. Ching, N. Bansal, ve B. Bhandari, "Alginate gel particles–A review of production techniques and physical properties", *Critical Reviews in Food Science and Nutrition*, c. 57, sy 6, ss. 1133-1152, Nis. 2017, doi: 10.1080/10408398.2014.965773.

[19] D. Dhamecha, R. Movsas, U. Sano, ve J. U. Menon, "Applications of alginate microspheres in therapeutics delivery and cell culture: Past, present and future", *International Journal of Pharmaceutics*, c. 569, s. 118627, Eki. 2019, doi: 10.1016/j.ijpharm.2019.118627.

[20] D. Hudson ve A. Margaritis, "Biopolymer nanoparticle production for controlled release of biopharmaceuticals", *Critical Reviews in Biotechnology*, c. 34, sy 2, ss. 161-179, Haz. 2014, doi: 10.3109/07388551.2012.743503.

[21] S. N. Pawar ve K. J. Edgar, "Alginate derivatization: A review of chemistry, properties and applications", *Biomaterials*, c. 33, sy 11, ss. 3279-3305, Nis. 2012, doi: 10.1016/j.biomaterials.2012.01.007.

[22] J. Ma *vd.*, "Magnetic graphene oxide-containing chitosan-sodium alginate hydrogel beads for highly efficient and sustainable removal of cationic dyes", *International Journal of Biological Macromolecules*, c. 193, ss. 2221-2231, Ara. 2021, doi: 10.1016/j.ijbiomac.2021.11.054.

[23] H. Zeng *vd.*, "Iron-loaded magnetic alginate-chitosan double-gel interpenetrated porous beads for phosphate removal from water: Preparation, adsorption behavior and pH stability", *Reactive and Functional Polymers*, c. 177, s. 105328, Ağu. 2022, doi: 10.1016/j.reactfunctpolym.2022.105328.

[24] M.-K. Zhang, X.-H. Zhang, ve G.-Z. Han, "Magnetic alginate/PVA hydrogel microspheres with selective adsorption performance for aromatic compounds", *Separation and Purification Technology*, c. 278, s. 119547, Ara. 2021, doi: 10.1016/j.seppur.2021.119547.

[25] B. Salahuddin *vd.*, "Magnetic Hydrogel Composite for Wastewater Treatment", *Polymers*, c. 14, sy 23, s. 5074, Kas. 2022, doi: 10.3390/polym14235074.

[26] S.-J. Wang *vd.*, "Floatable magnetic aerogel based on alkaline residue used for the convenient removal of heavy metals from wastewater", *Chemical Engineering Journal*, c. 399, s. 125760, Kas. 2020, doi: 10.1016/j.cej.2020.125760.

[27] Y. Wu *vd.*, "Construction of magnetic alginate-based biosorbent and its adsorption performances for anionic organic contaminants", *Separation and Purification Technology*, c. 297, s. 121566, Eyl. 2022, doi: 10.1016/j.seppur.2022.121566.

[28] J. Wang *vd.*, "Production of magnetic sodium alginate polyelectrolyte nanospheres for lead ions removal from wastewater", *Journal of Environmental Management*, c. 289, s. 112506, Tem. 2021, doi: 10.1016/j.jenvman.2021.112506.

[29] M. Mavaei, A. Chahardoli, Y. Shokoohinia, A. Khoshroo, ve A. Fattahi, "One-step Synthesized Silver Nanoparticles Using Isoimperatorin: Evaluation of Photocatalytic, and Electrochemical Activities", *Sci Rep*, c. 10, sy 1, s. 1762, Şub. 2020, doi: 10.1038/s41598-020-58697-x.

[30] S. Chkirida *vd.*, "Highly synergic adsorption/photocatalytic efficiency of Alginate/Bentonite impregnated TiO2 beads for wastewater treatment", *Journal of Photochemistry and Photobiology A: Chemistry*, c. 412, s. 113215, May. 2021, doi: 10.1016/j.jphotochem.2021.113215.

[31] J. Dai *vd.*, "TiO2-alginate composite aerogels as novel oil/water separation and wastewater remediation filters", *Composites Part B: Engineering*, c. 160, ss. 480-487, Mar. 2019, doi: 10.1016/j.compositesb.2018.12.097.

[32] S. Chkirida, N. Zari, R. Achour, A. E. K. Qaiss, ve R. Bouhfid, "Effect of iron doped titanium oxide encapsulated in alginate on photocatalytic activity for the removal of dye pollutants", *RSC Adv.*, c. 10, sy 38, ss. 22311-22317, 2020, doi: 10.1039/D0RA02898C.

[33] I. Hasan, C. Shekhar, W. Alharbi, M. Abu Khanjer, R. A. Khan, ve A. Alsalme, "A Highly Efficient Ag Nanoparticle-Immobilized Alginate-g-Polyacrylonitrile Hybrid Photocatalyst for the Degradation of Nitrophenols", *Polymers*, c. 12, sy 12, s. 3049, Ara. 2020, doi: 10.3390/polym12123049.

[34] N. Mundkur, A. S. Khan, M. I. Khamis, T. H. Ibrahim, ve P. Nancarrow, "Synthesis and characterization of clay-based adsorbents modified with alginate, surfactants, and nanoparticles for methylene blue removal", *Environmental Nanotechnology, Monitoring & Management*, c. 17, s. 100644, May. 2022, doi: 10.1016/j.enmm.2022.100644.

[35] K. Akin, V. Ugraskan, B. Isik, ve F. Cakar, "Adsorptive removal of crystal violet from wastewater using sodium alginate-gelatin-montmorillonite ternary composite microbeads", *International Journal of Biological Macromolecules*, c. 223, ss. 543-554, Ara. 2022, doi: 10.1016/j.ijbiomac.2022.11.002.

[36] M. Yari, P. Derakhshi, K. Tahvildari, ve M. Nozari, "Preparation and Characterization of Magnetic Iron Nanoparticles on Alginate/Bentonite Substrate for the Adsorptive Removal of Pb2+ Ions to Protect the Environment", *J Polym Environ*, c. 29, sy 7, ss. 2185-2199, Tem. 2021, doi: 10.1007/s10924-020-02028-8.